AD-A238 082

DTIC

ELECTE

JUL 0 3 1991

C

PL-TR-91-2013

SCATTERING AND POLARIZATION MEASUREMENTS USING THE PL/OPA LOW
ALTITUDE LIDAR

Richard C. Garner

PhotoMetrics, Inc.
4 Arrow Drive
Woburn, MA 01801-2067

20 December 1990

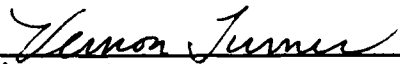•••Scientific Report No. 2•••

PHILLIPS LABORATORY
AIR FORCE SYSTEMS COMMAND
HANSCOM AIR FORCE BASE, MASSACHUSETTS 01731-5000
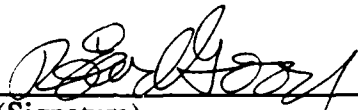
91-03944

"This technical report has been reviewed and approved for publication"

_____
(Signature)
Vernon Turner
Contract Manager

_____
(Signature)
Donald E. Bedo, Chief
Electro-Optical Measurements Branch

FOR THE COMMANDER

_____
(Signature)
R. Earl Good, SES, Director
Optical Environment Division

This report has been reviewed by the ESD Public Affairs Office (PA) and is releasable to the National Technical Information Service (NTIS).

Qualified requestors may obtain additional copies from the Defense Technical Information Center. All others should apply to the National Technical Information Service.

If your address has changed, or if you wish to be removed from the mailing list, or if the addressee is no longer employed by your organization, please notify GP/IMA, Hanscom AFB, MA 01731. This will assist us in maintaining a current mailing list.

Do not return copies of this report unless contractual obligations or notices on a specific document requires that it be returned.

REPORT DOCUMENTATION PAGE

1a. REPORT SECURITY CLASSIFICATION UNCLASSIFIED		1b. RESTRICTIVE MARKINGS	
2a. SECURITY CLASSIFICATION AUTHORITY		3 DISTRIBUTION / AVAILABILITY OF REPORT Approved for public release; distribution unlimited	
2b. DECLASSIFICATION / DOWNGRADING SCHEDULE N/A			
4 PERFORMING ORGANIZATION REPORT NUMBER(S) PhM-TR-91-06		5 MONITORING ORGANIZATION REPORT NUMBER(S) PL-TR-91-2013	
6a. NAME OF PERFORMING ORGANIZATION PhotoMetrics, Inc.	6b. OFFICE SYMBOL (If applicable)	7a. NAME OF MONITORING ORGANIZATION Phillips Laboratory	
6c. ADDRESS (City, State, and ZIP Code) 4 Arrow Drive Woburn, MA 01801-2067		7b. ADDRESS (City, State, and ZIP Code) Hanscom AFB, MA 01731-5000	
8a. NAME OF FUNDING / SPONSORING ORGANIZATION	8b. OFFICE SYMBOL (If applicable)	9. PROCUREMENT INSTRUMENT IDENTIFICATION NUMBER F19628-86-C-0102	

8c. ADDRESS (City, State, and ZIP Code)	10. SOURCE OF FUNDING NUMBERS			
	PROGRAM ELEMENT NO.	PROJECT NO.	TASK NO.	WORK UNIT ACCESSION NO.
	62101F	7670	15	AH

11. TITLE (Include Security Classification)

SCATTERING AND POLARIZATION MEASUREMENTS USING THE PL/OPA LOW ALTITUDE LIDAR

12. PERSONAL AUTHOR(S)
Richard C. Garner

13a. TYPE OF REPORT Scientific No. 2	13b. TIME COVERED FROM 860615 TO 900930	14 DATE OF REPORT (Year, Month, Day) 901220	15. PAGE COUNT 78

16. SUPPLEMENTARY NOTATION

17	COSATI CODES		18. SUBJECT TERMS (Continue on reverse if necessary and identify by block number)
FIELD	GROUP	SUB-GROUP	Lidar Remote Sensing Scattering
			Polarization Lidar Atmospheric Extinction

19. ABSTRACT (Continue on reverse if necessary and identify by block number)

This report describes the background theory, experimental techniques, and results of research relating to lidar polarization, scattering, and absorption effects using the GL/OP low altitude lidar system. The work, which is aimed at improving the understanding of lidar as a diagnostic tool for studying the atmosphere, has concentrated on understanding multiple scattering and scattering from irregularly shaped particles, and deducing the extinction coefficient from lidar data. We present results of polarization measurements in snow, Mie scattering calculations, extinction coefficient calculations and preliminary modeling of multiple scattering effects as applied to lidar experiments.

20 DISTRIBUTION / AVAILABILITY OF ABSTRACT ☐ UNCLASSIFIED/UNLIMITED ☒ SAME AS RPT ☐ DTIC USERS	21. ABSTRACT SECURITY CLASSIFICATION UNCLASSIFIED	
22a. NAME OF RESPONSIBLE INDIVIDUAL Mr. Vernon Turner, Contract Manager	22b. TELEPHONE (Include Area Code) 617/377-3650	22c. OFFICE SYMBOL PL/OPA

DD FORM 1473, 84 MAR   83 APR edition may be used until exhausted.   SECURITY CLASSIFICATION OF THIS PAGE

All other editions are obsolete.

UNCLASSIFIED

Contents

List of Figures

1 Introduction

This report describes the background theory, experimental techniques, and results of research relating to lidar polarization, scattering, and absorption effects which PhotoMetrics performed, under Contract F19628-86-C-0102, using the GL/OP low altitude lidar system. A companion report, hereafter in this report referred to as Part II, describes the upgrades and modifications PhotoMetrics made and provides an instruction manual for the operation of the lidar system.

PhotoMetrics has used the low altitude lidar system to gather data in support of GL's broad program aimed at modeling the optical properties of the lower atmosphere. The general approach we have taken in our research efforts has been in improving the understanding of lidar as a diagnostic tool for studying the atmosphere. We have concentrated this approach in three broad areas:

1. understanding the effects of multiple scattering in lidar experiments,

2. understanding the effects of scattering from irregularly shaped, randomly oriented particles, and

3. determining the validity and improving upon techniques of calculating the extinction coefficient from lidar data.

Sections 3 to 6 each report on major tasks undertaken during this program. Each has a bearing on one of the above three mentioned areas.

Section 2 gives a brief description of the lidar system and its measurement capabilities. A detailed description is given in Part II.

Section 3 describes our measurements of the polarization state of the backscattered 532 nm radiation. Most of these measurements have been done during falling snow conditions.

Section 4 gives a brief description of Mie scattering and discusses the results of a Mie scattering program that we have written for an MS-DOS based computer. This program was used in conjunction with understanding the validity of the lidar calculated extinction coefficient.

Section 5 describes our work on extinction. It describes the standard extinction algorithm, shows results when applied to lidar data, and describes some enhancements we have made.

Section 6 discusses our preliminary efforts of modeling multiple scattering effects in a lidar experiment.

Appendix A discusses and shows results of the field trip to the desert region of Dripping Spring, New Mexico in June, 1988. This trip was made in support of a measurement program at Sandia National Laboratory. This section also discusses the minimum calculable extinction coefficient as a function of the characteristics of a lidar system. These calculations were motivated by the Dripping Spring field trip.

2 Lidar Parameters

The GL/OP mobile, low altitude lidar is a biaxial system with the receiver mounted adjacent to the transmitter. The combination is housed in a temperature controlled enclosure which is mounted on a steerable trunion on top of a trailer. The data acquisition and control systems are located inside the trailer.

The laser transmitter is a Nd:YAG operating at 20 Hz. The primary output at 1.06 μm is 120 mJ/pulse. With a temperature-tuned CD*A crystal 25 mJ/pulse of the primary is converted to 0.53 μm. The laser pulse is approximately 15 ns in length. The beam divergence is approximately 2.5 mrad. The output is nearly 100% polarized.

The receiver is an f/1.3 refractive telescope with a 15 cm diameter aperture and a 10 mrad field of view. The transmitter/receiver crossover point is at 150 m. A gated photomultiplier tube detects 0.53 μm radiation through a 10Å bandwidth filter. For most of the work described in this report the PMT was operated in current mode, although it will simultaneously operate in photon counting mode (described in Part II). A silicon avalanche photodiode detects 1.06 μm radiation through a 10 nm bandwidth filter. The polarization state of the backscattered 0.53 μm radiation can be determined with a polarizer wheel located inside the receiver.

The data acquisition system consists of a CAMAC crate interfaced to an 80386 computer. For each channel, signal averaging is performed by a special CAMAC av-

eraging memory directly interfaced to a transient recorder. The transient recorders are 12 bit with an 8192 word memory and can acquire data at rates up to 20 Mhz. We typically run the transient recorders at 10 MHz. The signal averagers are 24 bit and will accumulate data for up to 65536 laser shots.

3 Polarization Studies

3.1 Introduction

PhotoMetrics designed and implemented a system to measure the polarization state of the backscattered 532 nm radiation. The details of the system and its method of operation are given in Part II.

Here we describe the polarization studies that we performed. Our most extensive work was done for falling snow. Section 3.2 provides the theoretical background for the polarization measurements. Section 3.3 describes the general qualitative features of the polarization state of backscattered lidar radiation. Section 3.4 describes our studies of falling snow, both experimental and theoretical.

Knowledge of the polarization state of the radiation, together with multiple scattering models, is necessary in order to determine the true extinction coefficient. A medium in which there is a large amount of multiple scattering has a smaller extinction coefficient than would otherwise be calculated by assuming single scattering (there is more backscattered radiation measured than is accounted for theoretically). Furthermore, since there are more multiple scatters as the radiation penetrates deeper into the medium, the extinction calculation using single scatter assumptions becomes less accurate.

Knowledge of the degree of polarization, together with previous experiments or models, can be used to identify the scattering particles. The degree of polarization of backscattered radiation from a medium composed of irregularly shaped particles is characteristic of the particular particles. For example, snowflakes will induce a greater amount of depolarization than the hexagonally shaped ice crystals of cirrus clouds because of the wider distribution of randomly oriented surfaces within a snowflake. The radiation in snow generally reflects many more times off several surfaces of the same snowflake before scattering. Thus, single scattering from a

3

snowflake can be viewed as multiple scattering within that snowflake.

3.2 Theoretical Background

The polarization state of electromagnetic radiation (coherent or incoherent, monochromatic or nonmonchromatic) is completely specified by its four Stokes parameters. These four parameters (the set is not unique) describe

1) the fraction of radiation which is in a single polarization state (i.e., the degree of polarization),

2,3) the amplitudes of two perpendicular components of the electric (or magnetic) field of the polarized portion of the radiation, and

4) the phase between these two components.

For a quasi-monochromatic wave described by

$$\vec{E} = [E_x(t)\hat{x} + E_y(t)\hat{y}]\,e^{i(kz-\omega t)} \tag{1}$$

where

$$
\begin{aligned}
E_x &= \epsilon_x(t)e^{i\phi_x(t)} \\
E_y &= \epsilon_y(t)e^{i\phi_y(t)}
\end{aligned}
\tag{2}
$$

and $E_{x,y}(t)$ are slowly varying compared to $e^{-i\omega t}$, four commonly used Stokes parameters are [1]

$$
\begin{aligned}
I &= \langle E_x E_x^* \rangle + \langle E_y E_y^* \rangle = \langle \epsilon_x^2 + \epsilon_y^2 \rangle \\
Q &= \langle E_x E_x^* \rangle - \langle E_y E_y^* \rangle = \langle \epsilon_x^2 - \epsilon_y^2 \rangle \\
U &= \langle E_x E_y^* \rangle + \langle E_x^* E_y \rangle = \langle 2\epsilon_x \epsilon_y \cos(\phi_x - \phi_y) \rangle \\
V &= i\left[\langle E_x E_y^* \rangle - \langle E_x^* E_y \rangle\right] = \langle 2\epsilon_x \epsilon_y \sin(\phi_x - \phi_y) \rangle.
\end{aligned}
\tag{3}
$$

The symbol $\langle \cdots \rangle$ denotes time average and "*" denotes complex conjugation. In addition, it was assumed that $\epsilon_{x,y}$ and $\phi_{x,y}$ are real quantities. The intensities of light polarized in the x and y directions are ϵ_x^2 and ϵ_y^2, respectively.

If the radiation is completely polarized then

$$Q^2 + U^2 + V^2 = I^2 \tag{4}$$

4

and there are therefore only three independent parameters. More generally, a portion of the radiation has random polarization which gives the relation

$$Q^2 + U^2 + V^2 < I^2. \tag{5}$$

A useful parameter is the degree of polarization defined as

$$\delta = \frac{\sqrt{Q^2 + U^2 + V^2}}{I} = \frac{I_p}{I_p + I_u}, \tag{6}$$

where $I_p \equiv \sqrt{Q^2 + U^2 + V^2}$ is the intensity of the polarized portion and $I_u \equiv I - I_p$ is the intensity of the unpolarized portion of the radiation.

It is illuminating to visualize the normalized quantities Q/I, U/I, and V/I as axes of a three dimensional cartesian coordinate system, as shown in Fig. 1. The polarization state of the radiation is then represented by a vector $(\frac{Q}{I}, \frac{U}{I}, \frac{V}{I})$ which lies inside or on the unit sphere (referred to as the Poincaré sphere [2]). The length of the vector is the degree of polarization. The component of the vector in the $\frac{Q}{I} - \frac{U}{I}$ plane is the degree of linear polarization (defined as $[Q^2 + U^2]^{1/2}/I$). The component of the vector along the $\frac{V}{I}$ axis is the degree of circular polarization. Other quantities, such as ellipticity and azimuth of the polarized portion of the radiation are also easily visualized.

An important property of the Stokes parameters for lidar work is that the Stokes parameters of the total radiation equal the sum of the Stokes parameters for the individual parts. With lidar we observe, during each digitization period of the data acquisition system, the total backscattered radiation from many scatters within a volume of atmosphere. The light from each scatterer is described by its own set of Stokes parameters. At the receiver all the backscattered radiation combines and has a new set of Stokes parameters. If radiation from the different scatterers is uncorrelated, as is usually the case for atmospheric scattering, then the Stokes parameters are additive:

$$\begin{pmatrix} I \\ Q \\ U \\ V \end{pmatrix} = \sum_i \begin{pmatrix} I_i \\ Q_i \\ U_i \\ V_i \end{pmatrix}. \tag{7}$$

The set of four measurements required to determine the four Stokes parameters of the backscattered radiation is not unique. In the low altitude lidar system we
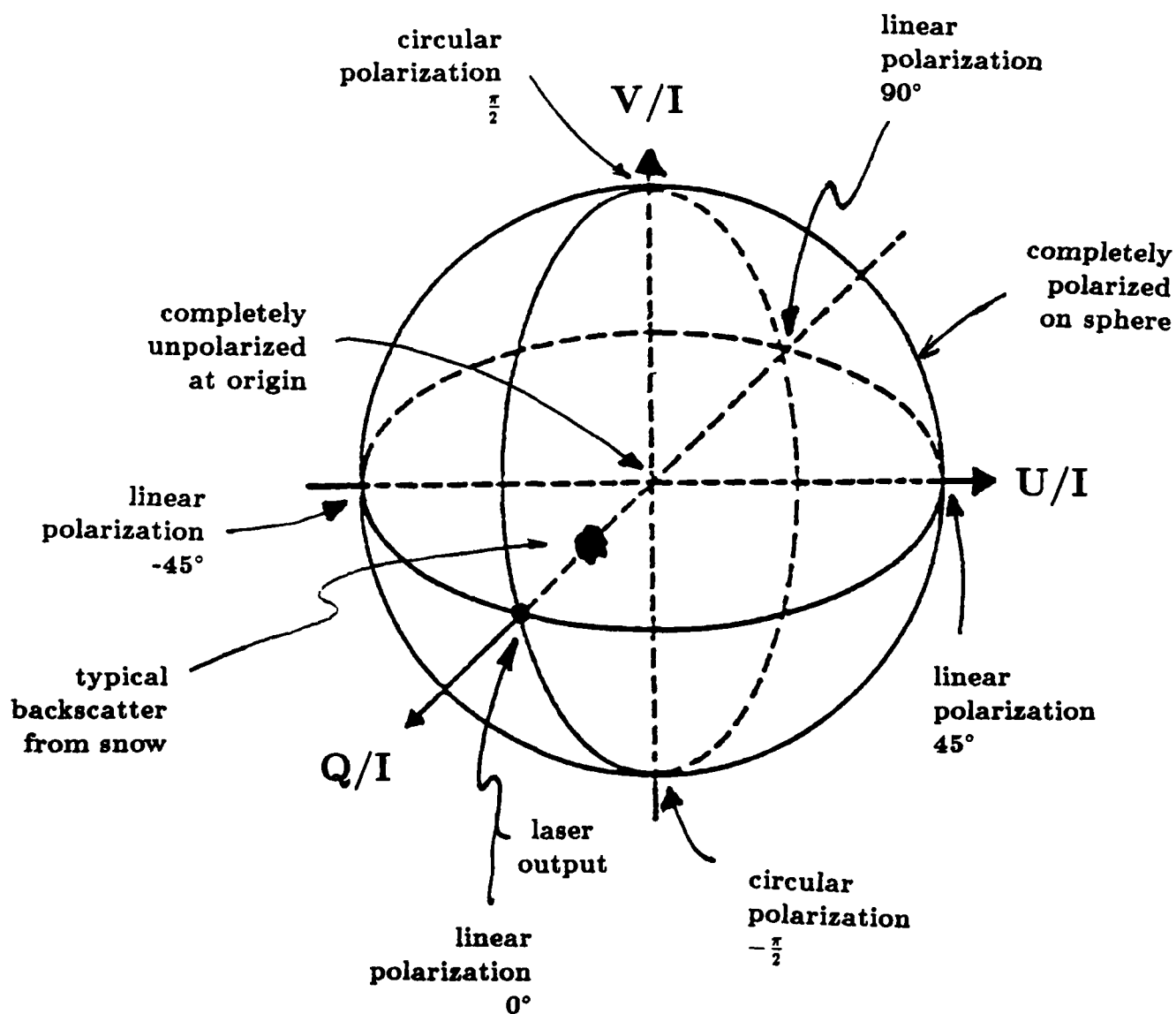
Figure 1: The Poincaré sphere: a geometrical interpretation of the Stokes parameters.

make the following four measurements (referenced to the laser output, which is nearly 100% linearly polarized and represented by the Stokes vector $[I, I, 0, 0]$):

$I_\parallel$: intensity polarized parallel to the laser output,

$I_\perp$: intensity polarized perpendicular to the laser output,

I_{45}: intensity polarized 45° to laser output, and

$I_\odot$: one of the circularly polarized components.

The Stokes parameters of the backscattered light are then

$$
\begin{aligned}
I &= I_\parallel + I_\perp \\
Q &= I_\parallel - I_\perp \\
U &= 2I_{45} - I_\parallel - I_\perp \\
V &= 2I_\odot - I_\parallel - I_\perp
\end{aligned}
\tag{8}
$$

A scattering event is described as an incident 4×1 Stokes vector being transformed into a scattered 4×1 Stokes vector. If the scattering is linear (i.e., if the scattering does not depend on the electric or magnetic field strengths, which is generally the case for situations of interest to us) then a 4×4 matrix (the scattering matrix), which is a function of scattering angle, represents the transformation. Only seven independent parameters are needed to specify the sixteen component matrix.

3.3 General Behavior of Backscattered Radiation

Backscattered radiation from spherical particles of all sizes (e.g., many types of aerosols and water droplets in cumulus clouds) and Rayleigh backscattered radiation (i.e., scattering from particles small compared to the wavelength) retain the polarization of the incident light.[1] In such cases the cylindrical symmetry about the axis defined by the laser beam prevents coupling to a different polarization state.

The backscattered radiation received by a lidar changes its polarization state relative to that of the incident radiation if

• the radiation multiple scatters or

---

[1]For Rayleigh scattering from particles with nonzero dipole moment the polarization state of backscattered radiation can change relative to the incident radiation. However, this is usually a small effect and is neglected in lidar work.

- the radiation single scatters from many irregularly shaped, randomly oriented particles.

The first situation occurs in most clouds, where the optical thickness (extinction coefficient times path length) is greater than one. The second situation occurs in cirrus clouds (hexagonal ice crystals), falling snow, and with some types of aerosols.

In both situations, if the laser output is completely polarized then the backscattered radiation generally is partially polarized, or has a degree of polarization less than one. The polarized portion of the radiation will, on average (i.e., for many laser pulses), be in the same polarization state as the incident light (with some spread about this average). From the point of view of the Poincaré sphere, the scattered vector is parallel to the incident vector, but smaller in magnitude.

For these situations two measurements, instead of four measurements, are sufficient to to determine the polarization state of the backscattered light.[2] For linearly polarized incident light, represented by vector $(1, 0, 0)$ on the Poincaré sphere, the scattered vector would be $(Q/I, 0, 0)$, where $Q/I < 1$. The quantity Q/I in this situation is both the degree of polarization and the degree of linear polarization. Thus, two sufficient measurements may be the polarization components of the backscattered light parallel and perpendicular to the polarization of the incident light. The values I and Q can be determined from these two measurements.

The spread in the polarization state about the average value, mentioned above, may be a valuable piece of information needed to characterize the scattering medium. For scattering from irregularly shaped, randomly oriented particles, the spread represents the fact that each single scatter may change the polarization state slightly, but the random orientation does not allow a preferred shift of the average. The size of the spread is reduced in proportion to the square root of (the number of scatterers in the receiver viewing volume multiplied by the number of laser shots in the lidar run). The complete set of four polarization measurements is needed to determine the spread. We have not made use of this information in our studies.

---

[2] Four measurements are only needed if the polarized portion of the scattered radiation is in a different state from that of the incident radiation, such as for single scattering from a single irregularly shaped particle, or from many irregularly shaped, *oriented* particles.

3.4 Falling Snow

3.4.1 Motivation

The identification of cirrus clouds, particularly high, thin, subvisible cirrus clouds, was the impetus for implementing the polarization detection system. As described in Section 3.3, the backscattered radiation from the hexagonal shaped ice crystals of cirrus is expected to have an unpolarized component. Further depolarization occurs due to multiple scattering.

Unfortunately, clouds are relatively quickly varying media. We have observed that many types of clouds will either change their physical shapes or drift within a few seconds. A full polarization measurement, consisting of four 5-10 second lidar runs (100-200 laser shots), usually cannot be made within this time. Even a two lidar run polarization measurement takes too long, unless we are willing to sacrifice signal-to-noise by averaging over fewer laser shots. The best we can hope for, in the current setup, is to get an average polarization measurement through the cloud.[3]

Falling snow is an excellent alternative to clouds in studying polarization effects. Falling snow is a relatively slowly varying medium. Snow density may vary as quickly as a few seconds, but as slowly as several minutes. Falling snow typically has a smaller extinction coefficient than clouds, providing a longer range over which single scattering can be observed separately from multiple scattering effects. The irregularly shaped, randomly oriented snowflakes display the depolarization effects of single scattered light quite nicely. In addition, since snow falls to the ground, other ground based diagnostics may be used to collect companion data for correlation and additional information.

Sections 3.4.2 to 3.4.5 describe our experimental and theoretical work on snow scattering. Section 3.4.2 presents observations and conclusions from lidar data acquired during falling snow conditions. Section 3.4.3 discusses our work on determining the maximum range of usefulness of lidar data for polarization calculations. Section 3.4.4 presents a scenario for snowflake scattering that we have formulated based our observations and conclusions. Section 3.4.5 describes the modeling that

---

[3] We have designed a polarization system, to be implemented in a new lidar receiver, which makes near simulaneous measurements of the four polarisations. This system is described in Part II.

9

we have done to describe single snowflake scattering.

3.4.2 Experiment

Lidar experiments performed in falling snow indicate that

- the degree of polarization of backscattered radiation is in the range of 0.3–0.5 and is fairly insensitive to snow density and

- the polarized portion of the backscattered radiation is, on average, in the same polarization state as the incident radiation.

Below we present the results of data analysis which support these conclusions. We also present a scenario for snowflake scattering based on these data and conclusions.

Figure 2a shows four successive lidar returns from falling snow. Each return corresponds to one of the four polarization measurements of Eq. 8.

These snow returns are four of several hundred returns taken over a four hour period on Feb. 4, 1988. During this period the snowfall rate, calculated from data obtained with a Particle Measurement System (PMS) rain distrometer, varied from zero to 80 $cm^{-2}sec^{-1}$.

Figure 2b shows the Stokes parameters and degree of polarization calculated from these data. For all data acquired on Feb 4, 1988 these calculations are performed in the manner prescribed by Eqs. 8 and 6.

For comparison Fig. 3 shows the Stokes parameters calculated from data acquired during clear air conditions. The degree of polarization for clear air is near unity because most of the scatterers are spherically shaped aerosols.

Figures 4 through 6 show plots of the Stokes parameters and the degree of polarization versus snow density and versus extinction coefficient at different ranges for all the lidar returns of Feb. 4, 1988. Snow density is calculated from snow rate obtained from the rain distrometer by assuming a snow velocity of 50 cm/sec. The extinction coefficient is determined using the Klett inversion routine on the lidar data. We discuss these calcualations, and their validity, in more detail in Section 5.3.2 on page 49.
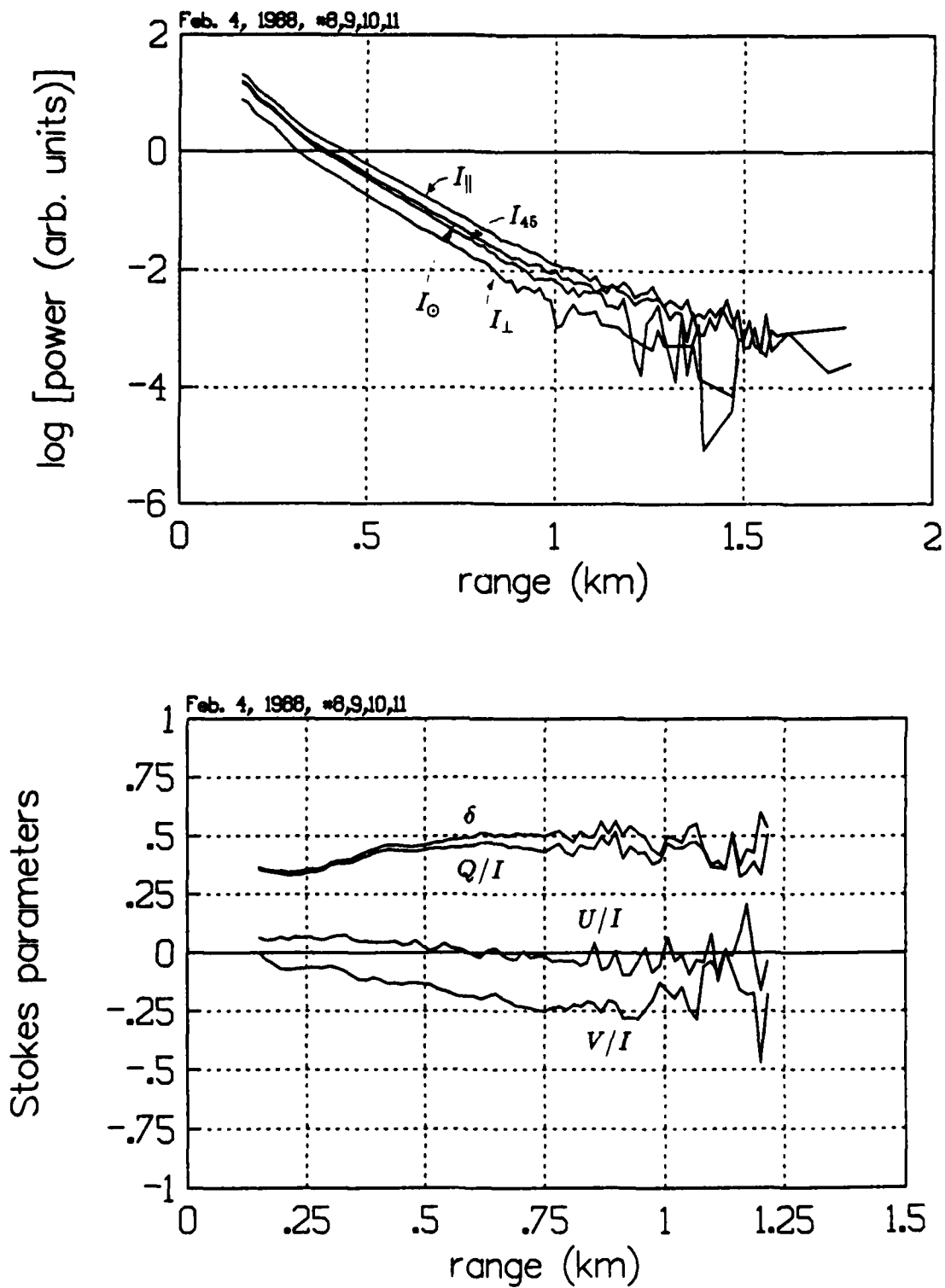
10

Figure 2: a) Four successive lidar returns from falling snow. b) Stokes parameters and degree of polarization calculated from these data.
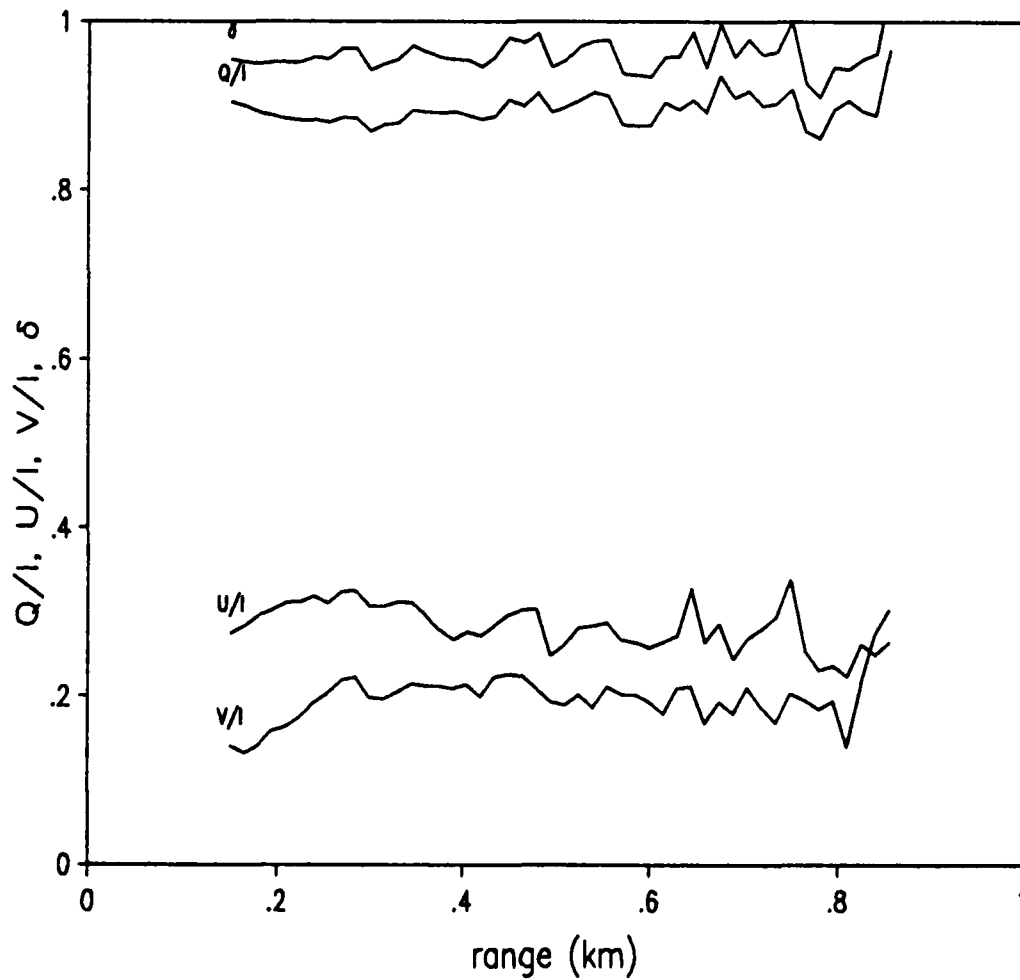
Figure 3: Stokes parameters and the degree of polarization calculated from data during clear air conditions.

12

Figure 7 shows a plot of the range-averaged value of Q/I versus the range-average value of extinction. The averages are computed over the interval 200–500 m. The value Q/I is equal to the degree of linear polarization when the polarized portion of the radiation is in the same polarization state as that of the incident laser radiation.

Figure 8 shows plots of the parameter Q/I versus lidar run for several different ranges. All of the lidar runs for Feb. 4, 1988 are included.

Figures 4 to 7 show that the degree of polarization is insensitive to snow density or, equivalently, extinction coefficient. Furthermore, the parameters U/I and V/I do not contribute much to the degree of polarization, since the value Q/I is nearly equal to the degree of polarization. Therefore, the degree of *linear* polarization is approximately equal to the degree of polarization, which is approximately equal to Q/I. (Put another way, the degree of circular polarization is small).

Since the incident laser radiation is entirely Q/I (i.e., $U/I = V/I = 0$) then the backscattered radiation is merely depolarized, or given a random component of polarization. The part that remains polarized is in the same state as the incident radiation. This is true on average, since there is some spread in degree of polarization and Q/I.

Since the parameter Q/I is approximately equal to the degree of polarization we can use it as an indicator of the effects of snow on polarization of the backscattered radiation. Therefore, when discussing snow, we henceforth use the term degree of polarization to refer to the value Q/I.

The insensitivity of degree of polarization is also revealed by data acquired during the falling snow of Jan 29, 1990. Figure 9a is a plot of range-averaged Q/I versus range-averaged extinction for that day. The snow fall on this day varied from light to heavy (compare extinction coefficients of Jan. 29, 1990 to those of Feb. 4, 1988.)

Figure 9b is the same plot but for data acquired during the very light snow of Jan 15, 1990. The averages in Figs. 9a and 9b are performed over the interval 200–400 m. The extinction coefficients are determined with the Klett inversion routine.

The Jan. 29, 1990 data shows that the degree of polarization is insensitive to extinction coefficient for extinctions greater than approximately 0.5–1 km-1.

Figure 4: Stokes parameters and degree of polarization versus a) snow density and b) extinction coefficient at 150 m range.

Figure 5: Stokes parameters and degree of polarization versus a) snow density and b) extinction coefficient at 285 m range.

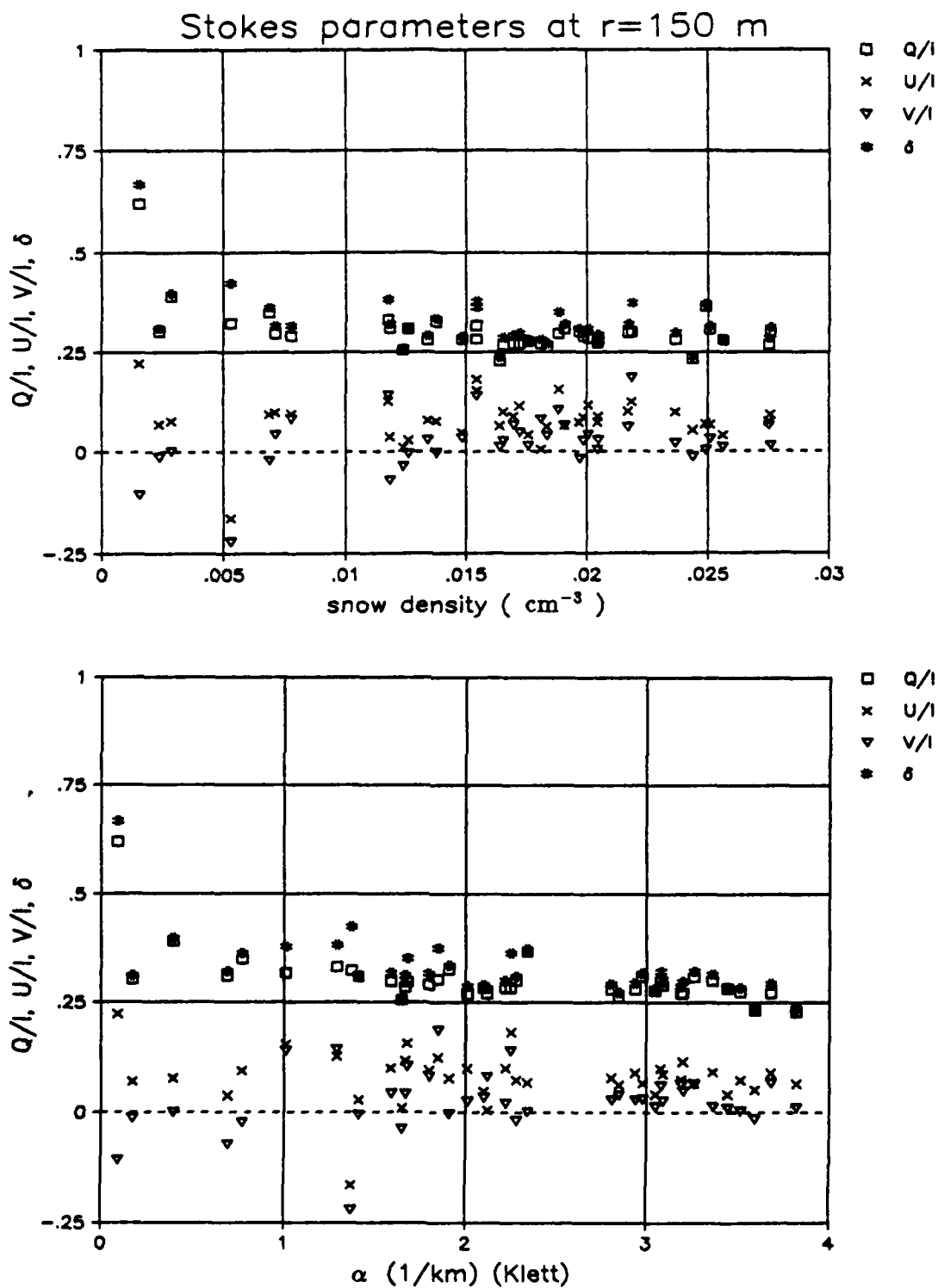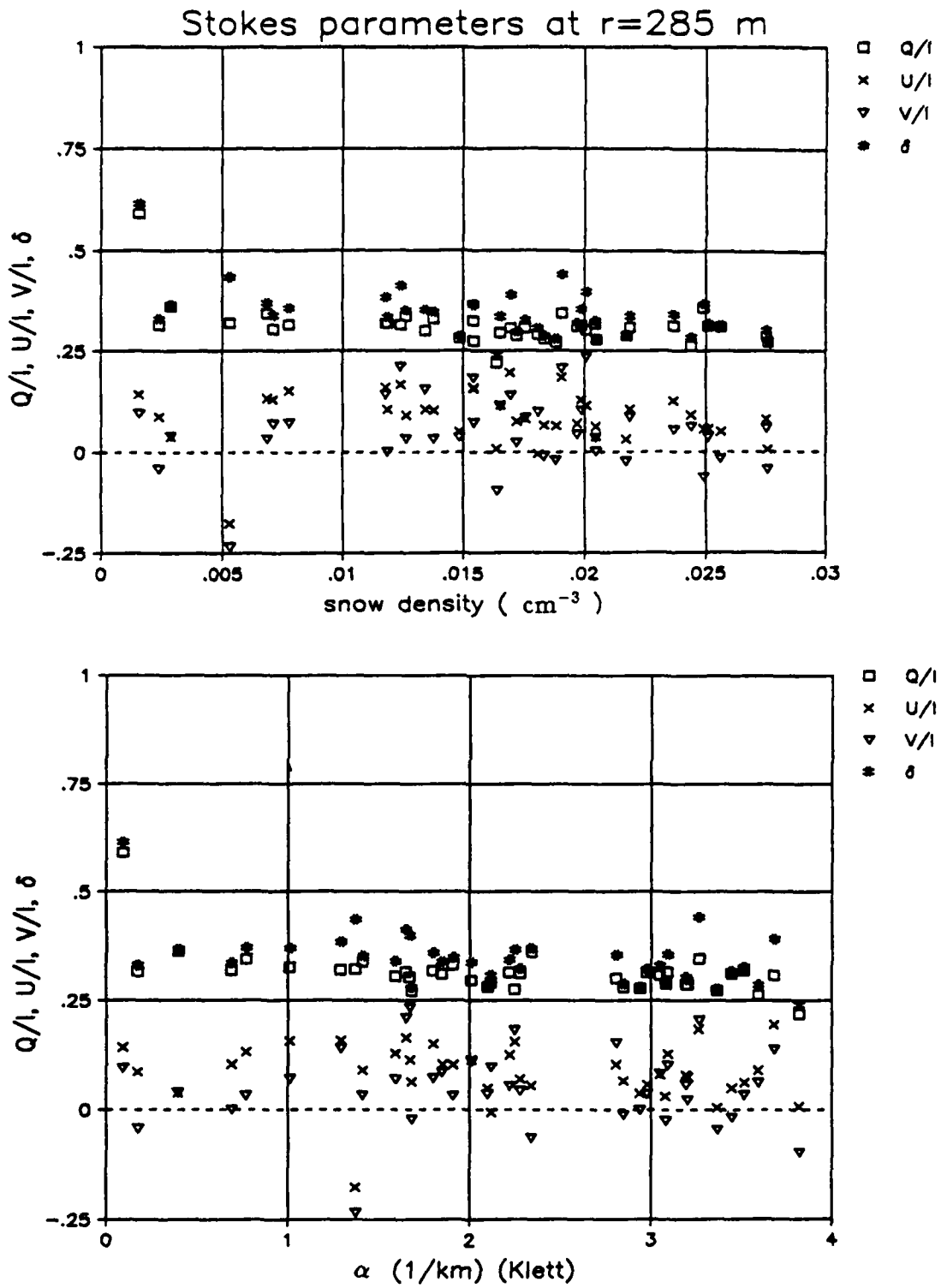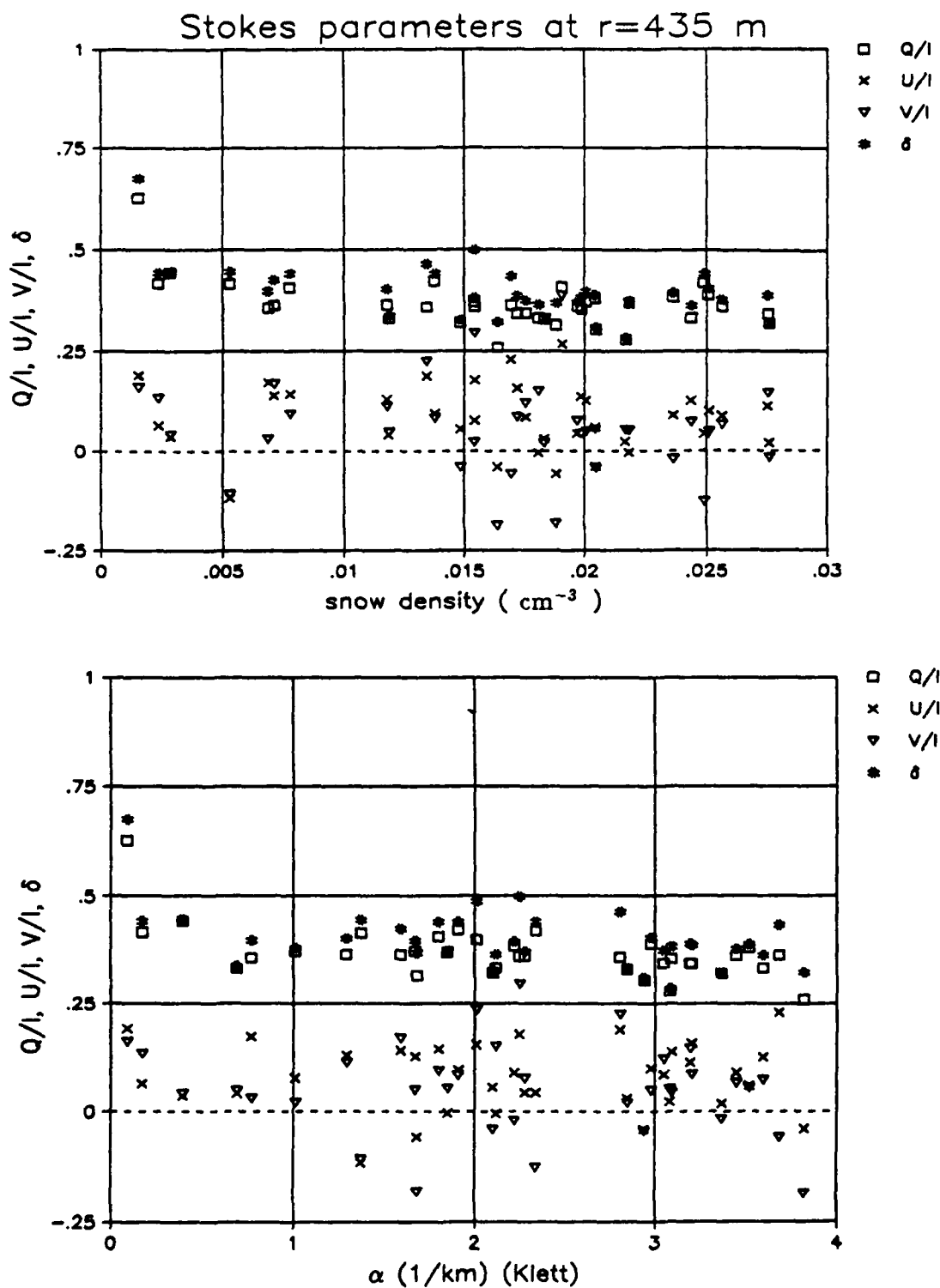Figure 6: Stokes parameters and degree of polarization versus a) snow density and b) extinction coefficient at 435 m range.
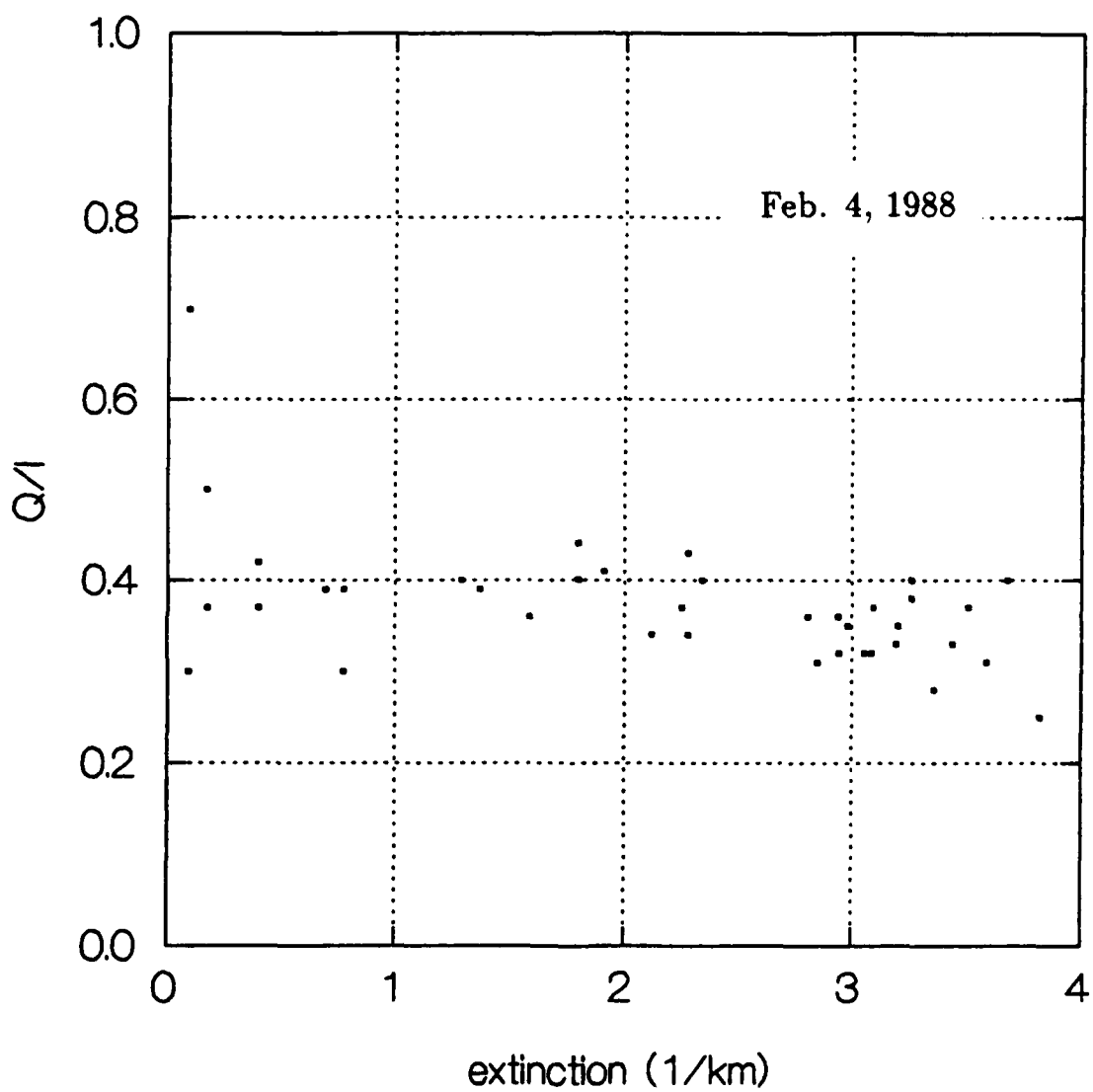
Figure 7: Average Q/I versus average extinction in the interval 200–500 m for Feb. 4, 1988 data.
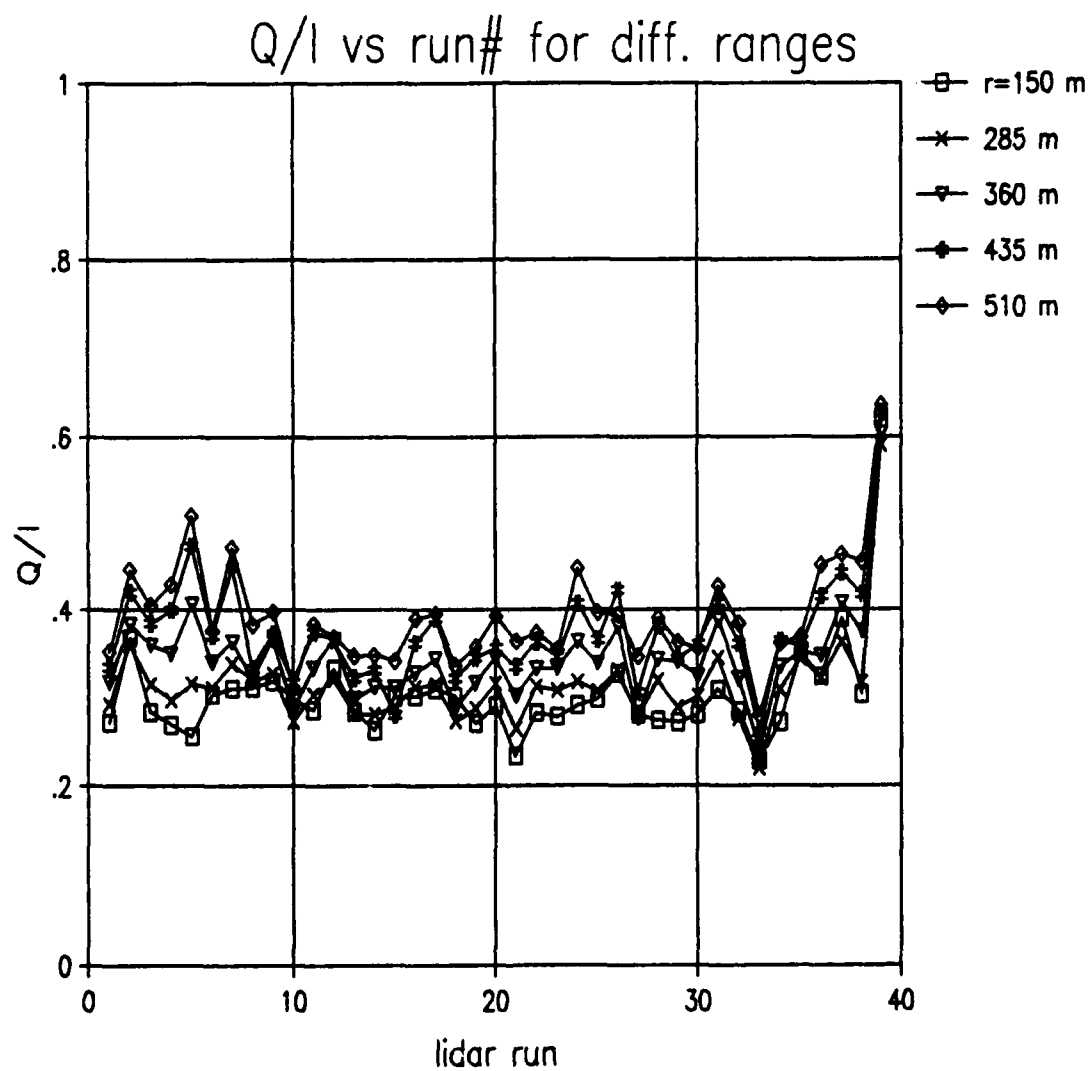
Figure 8: Q/I versus lidar run for different ranges.
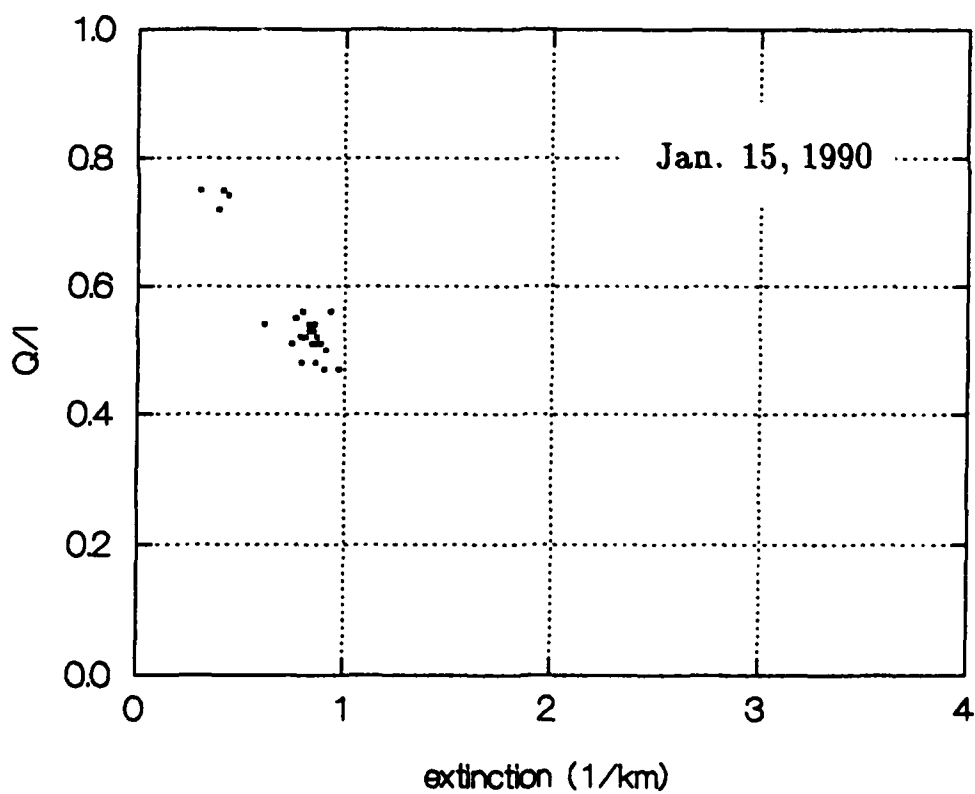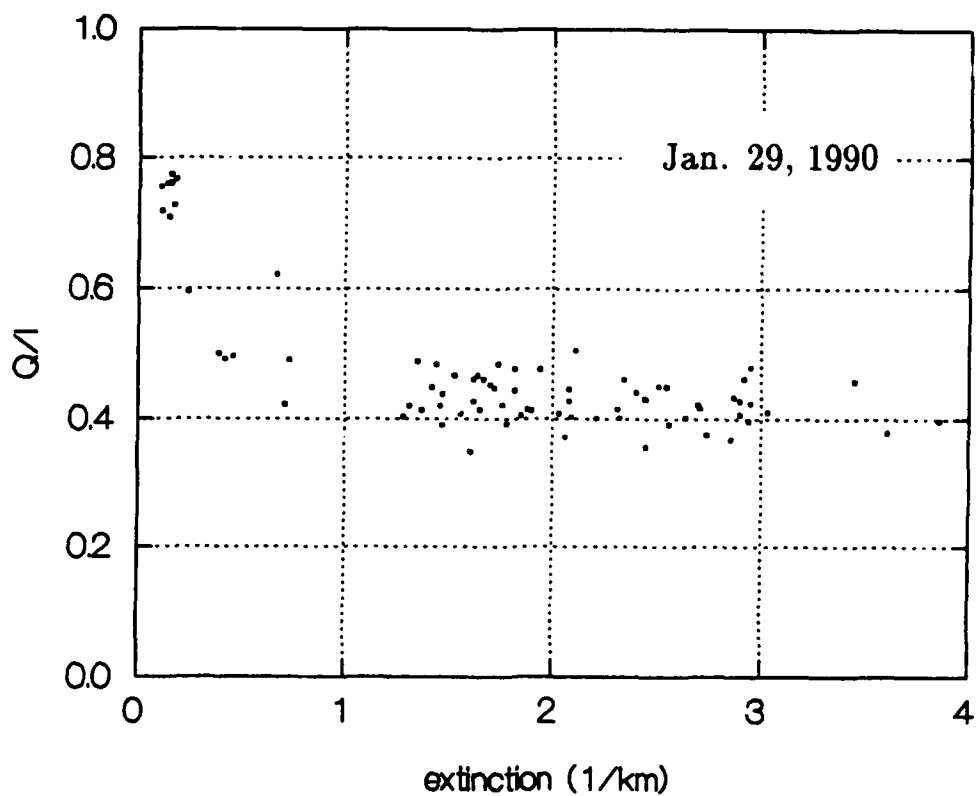
Figure 9: Average Q/I versus average extinction for a) Jan. 29, 1990 (light to heavy snow and b) Jan. 15, 1990 (light snow).

19

The Jan. 15, 1990 data does not have extinctions greater than these values and, therefore, it does not show the insensitivity of degree of polarization.

This sensitivity of degree of polarization at low snow density is explained by the fact that there are other constituents in the atmosphere during falling snow that do not depolarize the backscattered radiation. As the number of snow scatterers decrease, the fraction of these coherent scatterers increase. We discuss this in more detail below and in Section 3.4.5.

The value of Q/I for the data of Jan. 15, 1990 and Jan. 29, 1990 is determined differently from the way it was determined for the Feb. 4, 1988 data (for which we used Eq. 8). Since

$$\frac{Q}{I} = \frac{I_{\parallel} - I_{\perp}}{I_{\parallel} + I_{\perp}} = \frac{I_{\parallel}/I_{\perp} - 1}{I_{\parallel}/I_{\perp} + 1}$$

then Q/I can be determined from the slope of a plot of $I_{\perp}$ versus $I_{\parallel}$. Such a plot is shown for two lidar returns of Jan 29, 1990 in Fig. 10.

On this log-log plot the value of $I_{\parallel}/I_{\perp}$ is the vertical distance between the data and the line $I_{\parallel} = I_{\perp}$. For the actual data analysis we determine the value by calculating the slope of the least squares fit to the (non-logged) data. The uncertainty is then the standard deviation of the slope of the least squares fit.

Note the fairly constant slope up to approximately 1 km. Beyond 1 km the average (least squares) slope is approximately the same but the uncertainty increases due to greater uncertainty in the data.

3.4.3 Range of Validity of Lidar Data

We expect the degree of polarization to begin to decrease with range because multiple snowflake scattering should become more dominant. Although we do observe this decrease for many sets of lidar runs the decrease usually occurs beyond the range that we feel the lidar data is valid.

There is a danger in deriving quantities from lidar data that are too far out in range. As range increases signal-to-noise of course decreases. In addition, as signal decreases, the discreteness of the data imposed by the data acquisition system adds a different type of error.

20
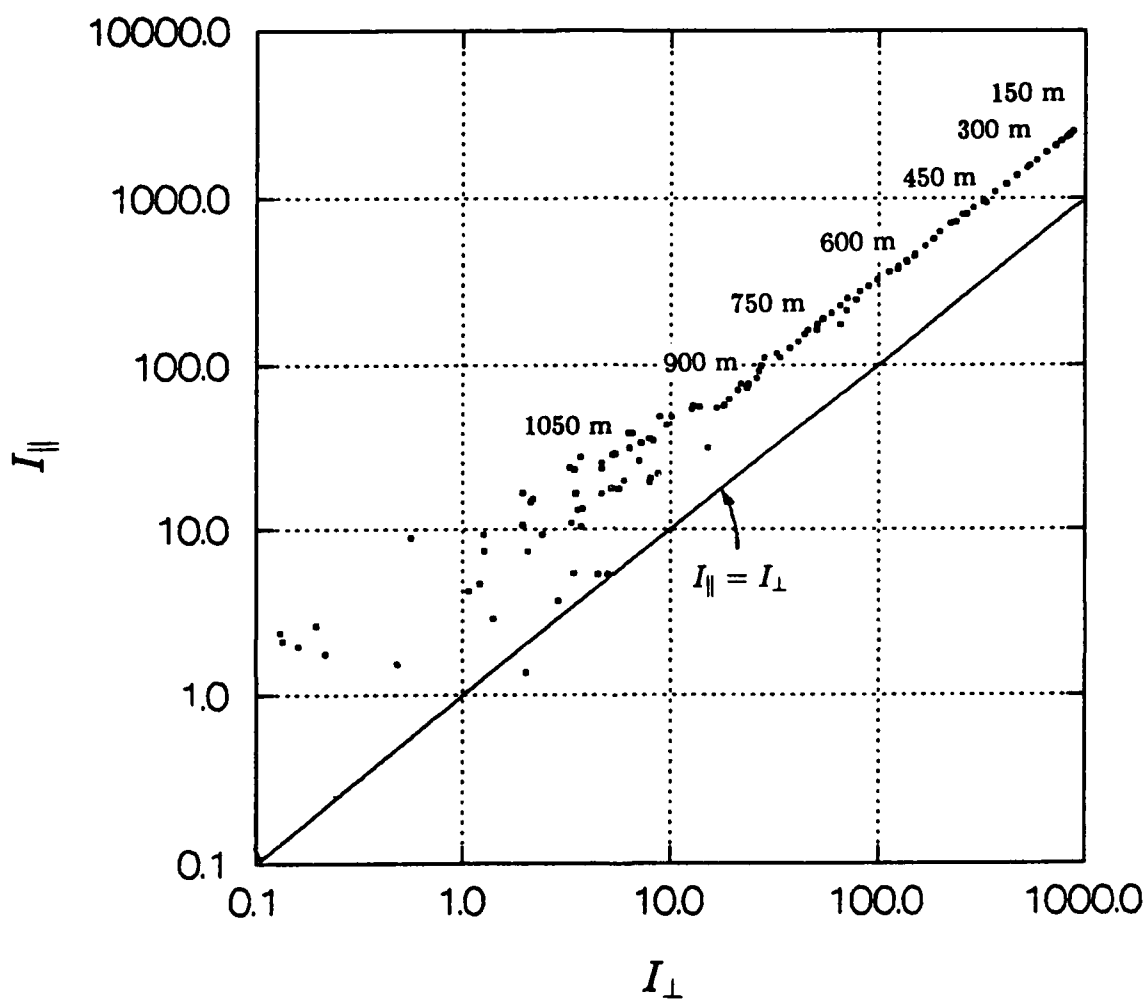
Figure 10: $I_\parallel$ versus $I_\perp$ for two successive lidar returns on Jan. 29, 1990.
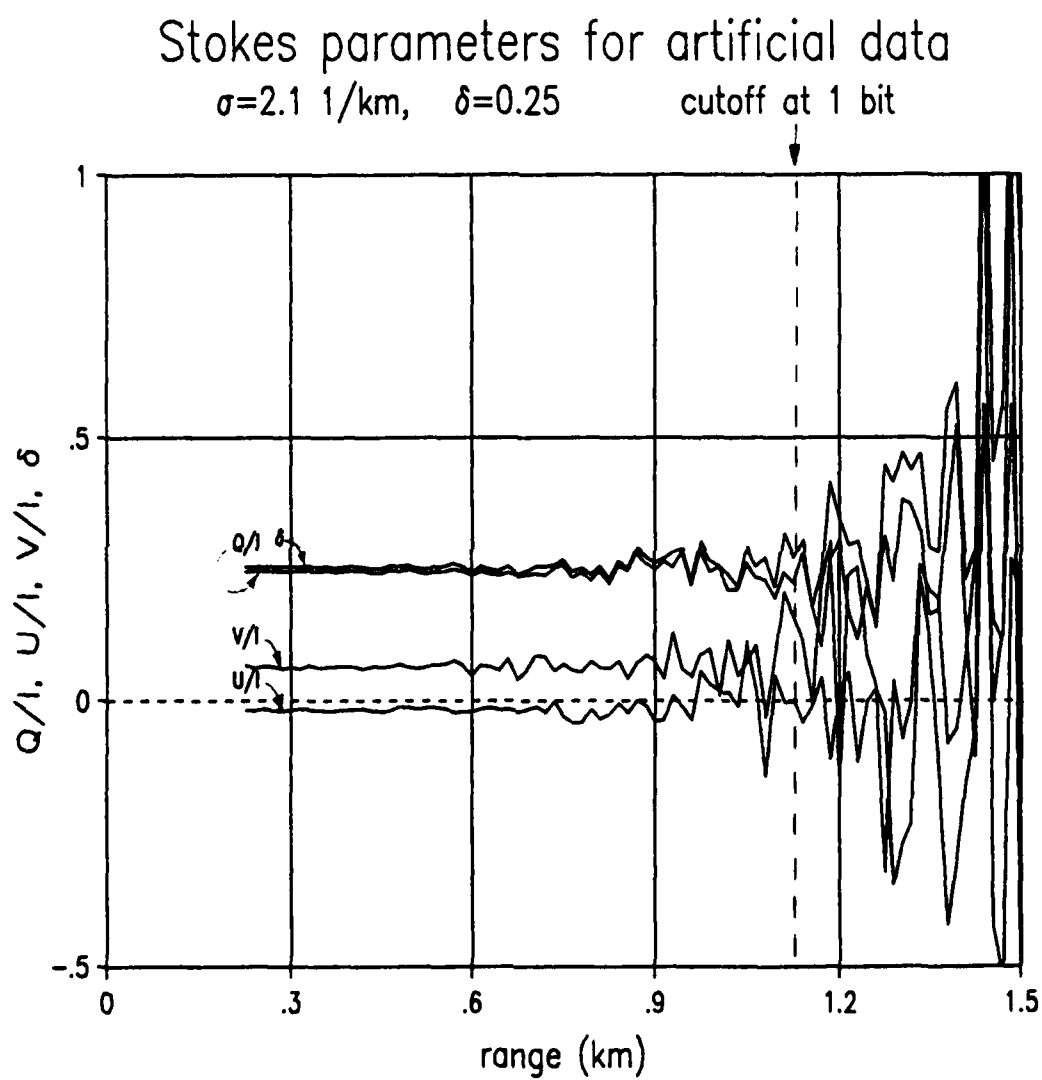
Figure 11: Stokes parameters for four simulated lidar returns.

We have checked, by computer simulation of the lidar, the validity of calculating degree of polarization from the lidar data at far ranges. Figure 11 shows the Stokes parameters for four simulated lidar returns corresponding to the four polarization measurements. These data were manufactured by making the following assumptions:

- The data obeys the single scatter lidar equation.

- The extinction coefficient is 2.1 km^{-1}, independent of range (similar to typical lidar runs during moderate snow).

- The backscatter coefficient is independent of range.

- The degree of polarization is 0.25, independent of range.

- The intensity of the polarization component of the lidar return parallel to that of the laser is 4000 (transient recorder units) at its peak. The transient recorder data word is 12 bits, corresponding to a dynamic range of 4096. The photomultiplier gain function is included in the analysis, which effectively increases the dynamic range (see Part II).

- The intensity of the other polarization components are chosen to be in the same proportion as one particular lidar run for which the degree of polarization is 0.25.

- Each individual return from 200 laser shots has Poisson noise added. In addition a background level with its own Poisson noise is added. The returns, with the noise, are then digitized and added to arrive at the total accumulated return.

Figure 11 indicates that the degree of polarization is valid out to the range where the signal minus the background becomes less than 1 bit. This is true for a wide range of degrees of polarization, signal levels, and background levels, as long as enough shots are averaged over so that the noise fluctuations are low enough. The discreteness imposed by digitization is the deciding factor. This is be expected since noise fluctuations are merely fluctuations about the "true" level. Taking enough

23

shots (if possible) should average this effect out. However, if a signal is less than 1 bit, and its fluctuation is smaller than the amount that would bring it up to 1 bit, then zero signal will be recorded, independent of number of laser shots.

The degree of polarization and Stokes parameters that we have shown in this report corresponds to the portions of lidar returns which are greater than 1 bit after the background is subtracted out.

3.4.4 Snowflake Scattering Scenario

We present a scenario for snowflake scattering based on the data and conclusions of Section 3.4.2. We divide snowflake scattering into two regimes: 1) single snowflake scattering (which we observe and have reported on above) and 2) multiple snowflake scattering (which we do not observe because of the lack of validity of the data at far ranges). In the first regime multiple snowflake scattering presumably occurs but is negligible. In the second regime multiple snowflake scattering is dominant.

The single snowflake scattering regime can be viewed as a multiple scattering phenomenon. From the point of view of a photon, each individual snowflake is a collection of surfaces with random orientation. A photon enters the snowflake region, reflects from or transmits through one or more of the surfaces, then leaves. Since snowflakes are large compared to the wavelength each reflection and transmission should be described fairly well by the Fresnel reflection and transmission coefficients (discussed in more detail in the theory Section 3.4.5).

Each reflection or transmission alters the polarization of the photon in a well defined way. Some interactions do not alter the polarization (e.g., a single backward reflection of linearly polarized incident light). Because of the large number of photons entering the snowflake region, and because of the randomness of the orientations of the surfaces, we expect that any photon changing its polarization state becomes one of many photons in one of the many polarization states different from the incident photon polarization state. These photons contribute to the unpolarized portion (random polarization) of the backscattered radiation. The photons that do not change their polarization state contribute to the polarized portion of the radiation.

24

Since this is statistical, we expect the degree of polarization to have a spread about some value. The spread should be smaller for greater numbers of snowflakes contributing to the backscatter signal. In the single snowflake scatter regime the received backscattered signal is the sum of backscattered signals from the many snowflakes in a viewing volume. This may be quite large. For example, for a digitization time of 0.1 μsec and a range of 200 m, the receiver viewing volume is 2.9 m^3. When the snow density is 0.015 cm^{-3} (midrange for the plots shown) there are 43500 snowflakes in this volume. The total number of snowflakes per viewing volume to be considered is this number times the number of laser shots being averaged over (200 for these data).

This number is large enough that we expect the degree of polarization to be quite insensitive to snow density. However, when the snow density is too low scattering from other particles that are present besides snowflakes becomes more prominent. If these particles cause the radiation to preserve its polarization upon backscatter, then the degree of polarization increases.

We must add a further comment due to a characteristic of the plot in Fig. 8. That plot shows Q/I versus lidar run (for all the runs of Feb. 4, 1988) for different ranges. Each range corresponds to a particular digitization by the transient recorders. The plot indicates that the degree of polarization increases with range up to 510 m. (For ranges greater than 510 m, which we do not show, the degree of polarization, when it can be calculated, is fairly constant and approximately equal to the 510 m value for each lidar run.)

We do not have a definite explanation for this observation. We hypothesize that the single snowflake phase function for the polarized portion of the radiation is highly peaked in the 180° direction, whereas the unpolarized portion is fairly isotropic. This is a reasonable assumption since the 180° direction is almost entirely composed of radiation that reflects off a snowflake surface that happens to be oriented perpendicular to the direction of propagation of the incident radiation. Therefore, as range increases the receiver views a smaller portion of the phase function centered in the 180° direction, or a higher proportion of radiation that is polarized.

3.4.5   Theory

The theoretical issues associated with the scenario described above can be separated into three parts:

1. single scattering from individual snowflakes (the fundamental interaction),

2. the sum of many single scatters in a receiver viewing volume, and

3. multiple snowflake scattering.

Each part requires the solution to the previous part, although each can be formulated indpendently. We have addressed parts 1 and 2 for snow scattering. We discuss these below. We have only addressed part 3, multiple scattering, for spherical particles. We discuss multiple scattering in Section 6.

Part 2: sum of many single scatters

We discuss part 2 first since we actually did this work first. We developed a Monte Carlo type model to predict the degree of polarization of the sum of radiation backscattered from the many snowflakes in a single lidar volume. The scattered radiation from an individual snowflake is assumed to be in a definite, although random, polarization state. Since we did not have a model for single snowflake scattering, we had to assume a probability of final states in a certain way, which we describe below. Adding the Stokes vectors from all the snowflakes in a viewing volume (see Eq. 7), and making the calculation many time, then gives a probability for the degree of polarization for the lidar return.

The calculation is performed in the following way:

- For each of N snowflakes, choose ϵ_x and ϵ_y, the intensity of the backscattered radiation, from each snowflake, polarized in the x and y directions respectively. Choose by assuming each amplitude to be random variables uniformly distributed on the interval $[0,1]$.

- For each of N snowflakes, choose the phase difference Δ between these two amplitudes by assuming it to be a random variable uniformly distributed on the interval $[-\pi, \pi]$.

26

- For each of N snowflakes, calculate the Stokes parameters.

- Choose a number M of scatterers which preserve the polarization state of the incident radiation (coherent scatterers). The Stokes vector for the backscattered radiation from each of these scatterers is $[1,1,0,0]$.

- Calculate the degree of polarization of light backscattered from snowflake and coherent scatterers in the following manner:

$$\delta = \frac{\left[\left(M + \sum_{i=1}^{N} Q_i\right)^2 + \left(\sum_{i=1}^{N} U_i\right)^2 + \left(\sum_{i=1}^{N} V_i\right)^2\right]^{1/2}}{M + \sum_{i=1}^{N} I_i} \qquad (9)$$

- Repeat

Figure 12 shows the result of a Monte Carlo calculation, performed on an 80286 based computer, for 10 snowflakes and 0 coherent scatterers. The figure shows plots of the probability density functions for the degrees of polarization, linear polarization, and circular polarization. The program was stopped when the probability curves looked reasonably smooth.

The degree of circular polarization, which is only shown for positive values, is actually symmetric about zero. This is because of the assumption that the probability of the phase difference between ϵ_x and ϵ_y is symmetric about zero phase.

Figures 13a and 13b show two plots which are a compendium of the information from many individual Monte Carlo calculations of type shown in Fig. 12. Figure 13a is a plot of the peaks of the probability curves for the degree of polarization, as a function of the ratio of coherently scattered power to power scattered by snowflakes, for different number of snowflakes in the viewing volume. The peak of each probability curve is approximately equal to the average of the probability curve. The plot in Fig 13b is similar, except that it shows the standard deviation of each probability curve.

If we choose one snowflake and zero coherent scatterers in the volume then there is a probability of one that the degree of polarization is one (since each scatter always results in a definite polarization state). Increasing the number of coherent

27

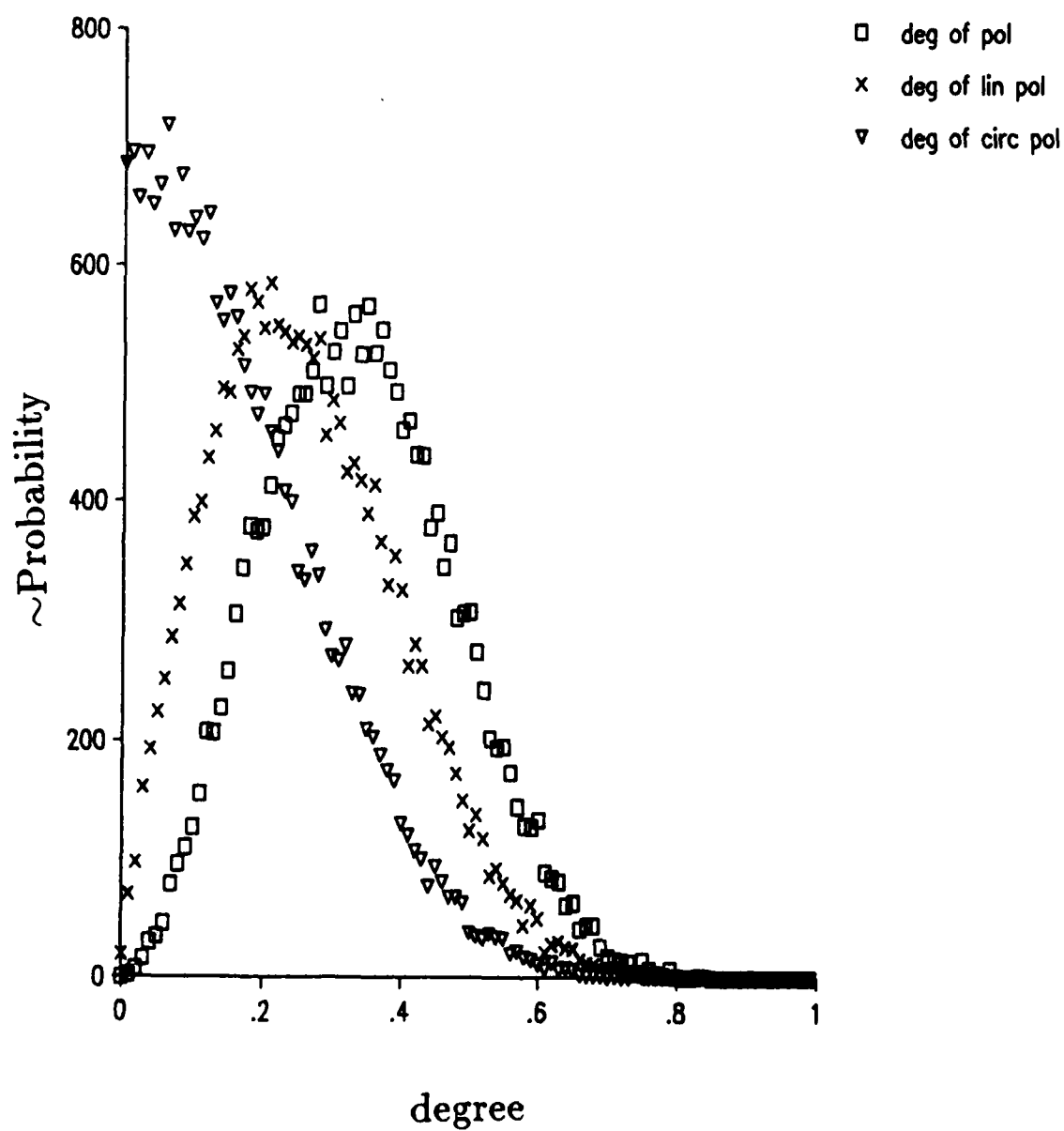Monte Carlo results for
10 snow particles
0 coherent scatterers

Figure 12: Monte Carlo calculation for 10 snowflakes and 0 coherenent scatterers.

Figure 13: a) Average and b) standard deviation of the degree of polarization versus ratio of the number of snow to coherent scatterers.

scatterers for a single snowflake at first decreases the most probable value of degree of polarization because a coherent scatter, by definition, always result in one particular polarization state (represented by the Stokes vector [1,1,0,0]).

As the number of snowflakes is increased, the most probable value of degree of polarization decreases. However, the standard deviation decreases as well.

As the number of snowflakes approaches infinity a plot of the most probable values of degree of polarization as a function of the ratio of coherent to snow backscattered power approaches the curve labeled "∞" on Fig. 13a. This result is expected due to the form of Eq. 6 which we rewrite here:

$$\delta = \frac{I_p}{I_p + I_u} = \frac{I_p/I_u}{I_p/I_u + 1} \tag{10}$$

The most probable value of degree of polarization for an infinite number of snowflakes and zero coherent scatterers is zero. That is, all the backscattered radiation from snow is randomly polarized. Therefore, I_u is all the radiation backscattered from snow. I_p is all the radiation backscattered from the coherent scatterers since this radiation is polarized and in the same state. The ratio I_u/I_p for an infinite number of snowflakes is therefore the ratio of snow to coherent backscattered power, the variable on the horizontal axis of Fig. 13a. The "∞" curve in that figure is simply a plot of δ versus I_u/I_p from Eq. 10.

We see that for the many thousands of snowflakes in a lidar receiver viewing volume (calculated in the previous section), it is valid to use the "∞" curve.

Part 1: single snowflake scattering

The results of a single snowflake scattering theory can, in principle, be used to determine the actual probability density functions for ϵ_x, ϵ_y, and Δ which are needed for the sum-of-single-scatters model given above. Recall that we assumed these random variables to be uniformly distributed on some range.

We have developed a preliminary model for single snowflake scattering, although we did not apply it to the sum-of-single-scatters model. As we determined above, the large number of snowflakes in a viewing volume allows us to assume that the degree of polarization lies on the "∞" curve shown in Fig. 13a. This assumption is valid as long as we choose probability density functions such that the average

30

degree of polarization decreases as snowflake density increases.

Our model for single snowflake scattering is based on the scenario we presented in Section 3.4.2 on page 24. The following list summarizes the scenario and the assumptions used by the model:

- Light that hits a snowflake undergoes a series of one or more transmissions and/or reflections from randomly oriented surfaces of the snowflake.

- The direction of the normal vector of one of these surfaces is a random variable distributed uniformly in solid angle (i.e., $P(\theta, \phi)d\Omega = 1/4\pi d\Omega$).

- Each interaction (reflection or transmission) is described by Snell's law and the Fresnel reflection and transmission coefficients.

- After a given interaction all the light which was reflected or transmitted is available for the next interaction.

- Light that changes polarization is considered part of the unpolarized portion of the backscattered light (I_u). Light that has polarization preserved is part of the polarized portion (I_p). The degree of polarization from the snowflake is then $\delta = I_p/(I_u + I_p)$.

Consider only the set of interactions that attenuate light the least (see Figs. 14a through 14c):

1. 1 reflection (preserves polarization),

2. 2 reflections (may change polarization), and

3. 1 transmission–1 reflection–1 transmission (may change polarization).

An additional reflection will attenuate the light further by an amount on the order of the average Fresnel reflectivity of 0.12 (averaged over angle of incidence and polarization).

We sum up the amount of polarized and unpolarized power from each of these interactions. Since the degree of polarization is only dependent on the ratio, we can assume an incident power of one.

a) 1 reflection

n = 1.33
n = 1

surface
(reflection)

E_r k_r

k_i

E_i

c) 1 transmission–1 reflection–1 transmission

n = 1
n = 1.33

2nd surface
(reflection)

k_2

E_2

n = 1.33
n = 1

k_1

E_1

3rd surface
(transmission)

1st surface
(transmission)

n = 1.33
n = 1

E_r

k_r

k_i

E_i

2nd surface
(reflection)

b) 2 reflections

n = 1.33
n = 1

1st surface
(reflection)

k_1

E_1

E_r

n = 1.33
n = 1

k_r

k_i

E_i
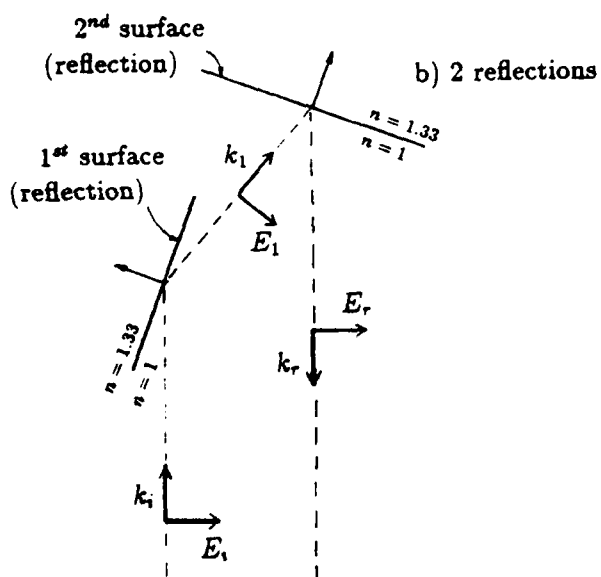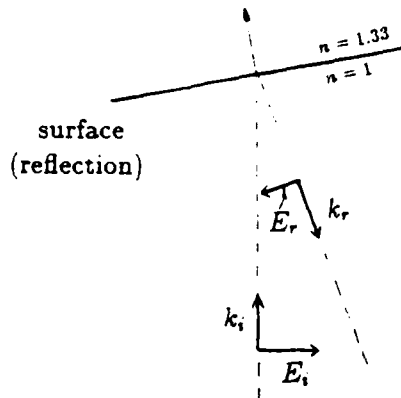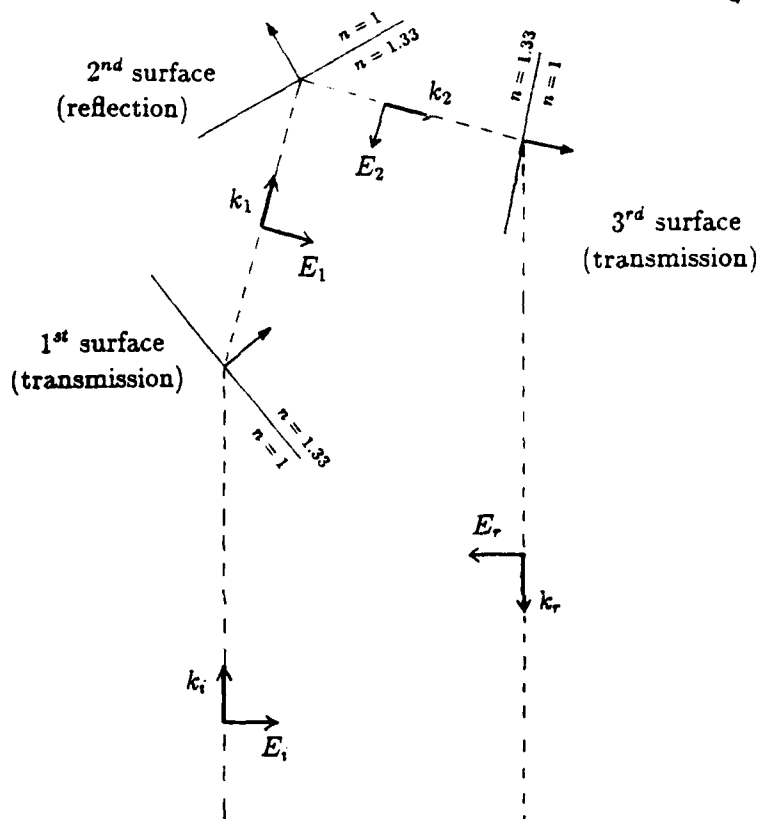
Figure 14: The three interactions considered for the single snowflake scatter model.

32

For the first two interactions above we analytically calculated the polarized and unpolarized backscattered power. For the third interaction we wrote a computer program on an 80386 based computer. An additional approximation we made in regard to the third interaction is discussed below.

The backscattered powers from each interaction are summarized below. α is the receiver field of view.

interaction	I_p	I_u
1	$6.1 \times 10^{-4} \, \alpha^2$	0
2	$4.6 \times 10^{-4} \, \alpha^2$	$4.2 \times 10^{-6} \, \alpha^2$
3	$1.6 \times 10^{-6} \, \alpha^2$	$8.0 \times 10^{-4} \, \alpha^2$

From this we calculate the degree of polarization:

$$\frac{I_p}{I_u} = \frac{6.1 \times 10^{-4} + 4.6 \times 10^{-4} + 1.6 \times 10^{-6}}{4.2 \times 10^{-6} + 8.0 \times 10^{-4}} = 1.3 \tag{11}$$

$$\delta = \frac{I_p/I_u}{1 + I_p/I_u} = 0.57 \tag{12}$$

The result of 0.57 for the degree of polarization is not far off from the 0.3–0.5 degree of polarization that we experimentally observe for single snow scattering (see Fig. 8 on page 18). That such an approximate theory would give a result within an order of magnitude is an indication that the basic assumed interactions must have some validity.

We must qualify our result for the intensity of the unpolarized radiation for the third interaction given above. The results of the computer calculation actually give a value of zero for I_u. The radiation that is scattered back to the receiver is completely polarized. A large majority of the radiation ($0.036\alpha^2$) is totally internally reflected at the third surface, and must go on to either interact with another surface or leave the snowflake region. We assumed that this radiation is an unpolarized, isotropic source of radiation for one additional reflection. Summing up all of this radiation that can get back to the receiver, making the same assumption as before about the random orientation of the surfaces, gives the above result for I_u for the third interaction.

4 Mie Scattering

4.1 Introduction

Mie scattering is the overall guiding theoretical mechanism for scattering in our lidar work. Although it is not always applicable, it is usually the best theory which is exactly soluble.

Early on in this program we studied Mie scattering, from the point of view of understanding its validity in our lidar experiments. In particular, we wanted to determine the validity of the widely used assumption that the extinction coefficient is proportional to the backscatter coefficient for a collection of Mie scatterers (e.g., aerosols) with a size distribution typical of the atmosphere.

We developed computer programs which calculate, for a range of particle sizes, the total Mie scattering cross section and the differential scattering cross section for a 180° scattering angle, and convolve these cross sections with arbitrarily chosen size distributions. Results are presented in Section 4.4. Section 4.2 is a background discussion of Mie scattering. It presents some theoretical background and concludes with expressions for the Mie scattering total cross section and differential scattering cross section for 180°. Section 4.3 describes our computer model.

4.2 Theoretical Background

Mie scattering refers to the scattering of a monochromatic electromagnetic plane wave by a spherically shaped, homogeneous, isotropic dielectric and conducting medium embedded in an infinite, homogeneous, isotropic, dielectric, nonconductiong medium. The analytic solution of this problem was published by Gustav Mie in 1908 [3]. It is the solution of Maxwell's equations with boundary conditions corresponding to the above scenario.

The electric field of the incident plane wave is assumed to be $\exp\left[i(k_1 z - \omega t)\right]\hat{x}$, where $k_1 = k_o n_1$, n_1 is the real-valued index of refraction of the infinite medium, and $k_o = \omega/c$ is the vacuum wave vector amplitude. The amplitude of the incident field is unity. Its polarization is in the x direction. The index of refraction n_2 of the sphere is complex.

The scattered electromagnetic field is the sum of two subfields. One subfield has

34

a magnetic field with zero radial component and the other subfield has an electric field with zero radial component. Each subfield is an infinite series solution to the equations and boundary conditions. The solution is cast in spherical coordinates.

The electric and magnetic fields of the first subfield (zero radial magnetic field), designated with a superscript ^{e}, are [2]

$$E_r^e = \frac{1}{k_1^2} \frac{\cos\phi}{r^2} \sum_{l=1}^{\infty} l(l+1) B_l^e \varsigma_l(k_1 r) P_{l,1}(\cos\theta)$$

$$E_\theta^e = -\frac{1}{k_1} \frac{\cos\phi}{r} \sum_{l=1}^{\infty} B_l^e \varsigma_l'(k_1 r) P_{l,1}'(\cos\theta) \sin\theta$$

$$E_\phi^e = -\frac{1}{k_1} \frac{\sin\phi}{r} \sum_{l=1}^{\infty} B_l^e \varsigma_l'(k_1 r) P_{l,1}(\cos\theta) \frac{1}{\sin\theta} \qquad (13)$$

$$H_\theta^e = \frac{i}{k_o} \frac{\sin\phi}{r} \sum_{l=1}^{\infty} B_l^e \varsigma_l(k_1 r) P_{l,1}(\cos\theta) \frac{1}{\sin\theta}$$

$$H_\phi^e = -\frac{i}{k_o} \frac{\cos\phi}{r} \sum_{l=1}^{\infty} B_l^e \varsigma_l(k_1 r) P_{l,1}'(\cos\theta) \sin\theta$$

The electric and magnetic fields of the second subfield (zero radial electric field), designated with a superscript ^{m} are [2]

$$E_\theta^m = \frac{i}{k_1} \frac{\cos\phi}{r} \sum_{l=1}^{\infty} B_l^m \varsigma_l(k_1 r) P_{l,1}(\cos\theta) \frac{1}{\sin\theta}$$

$$E_\phi^m = \frac{i}{k_1} \frac{\sin\phi}{r} \sum_{l=1}^{\infty} B_l^m \varsigma_l(k_1 r) P_{l,1}'(\cos\theta) \sin\theta$$

$$H_r^m = \frac{1}{k_1 k_o} \frac{\sin\phi}{r^2} \sum_{l=1}^{\infty} l(l+1) B_l^m \varsigma_l(k_1 r) P_{l,1}(\cos\theta) \qquad (14)$$

$$H_\theta^m = \frac{1}{k_o} \frac{\sin\phi}{r} \sum_{l=1}^{\infty} B_l^m \varsigma_l'(k_1 r) P_{l,1}'(\cos\theta) \sin\theta$$

$$H_\phi^m = \frac{1}{k_o} \frac{\cos\phi}{r} \sum_{l=1}^{\infty} B_l^m \varsigma_l'(k_1 r) P_{l,1}(\cos\theta) \frac{1}{\sin\theta}$$

In Eqs. 13 and 14

$P_{l,1}$ is an associated Legendre polynomial with $m = 1$,

$\varsigma_l(\rho) = \rho \left[j_l(\rho) - i y_l(\rho) \right]$,

j_l and y_l are the usual spherical Bessel functions,

"prime" (') denotes differentiation with respect to argument, and

the time dependence of each field component is $e^{-i\omega t}$.

The coefficients B_l^e and B_l^m, which are only functions of the permitivities and conductivity of the sphere and surrounding medium, are given by

$$B_l^e = i^{l+1} \frac{(2l+1)}{l(l+1)} \left[\frac{\hat{n}\psi_l'(q)\psi_l(\hat{n}q) - \psi_l(q)\psi_l'(\hat{n}q)}{\hat{n}\varsigma_l'(q)\psi_l(\hat{n}q) - \varsigma_l(q)\psi_l'(\hat{n}q)} \right]$$

$$B_l^m = i^{l+1} \frac{(2l+1)}{l(l+1)} \left[\frac{\hat{n}\psi_l(q)\psi_l'(\hat{n}q) - \psi_l'(q)\psi_l(\hat{n}q)}{\hat{n}\varsigma_l(q)\psi_l'(\hat{n}q) - \varsigma_l'(q)\psi_l(\hat{n}q)} \right] \tag{15}$$

where

$$\hat{n} = \frac{n_2}{n_1} = \left[\frac{\epsilon_2}{\epsilon_1} + i\frac{4\pi\kappa}{\omega\epsilon_1} \right]^{1/2} \tag{16}$$

and

$q = k_1 a$ ("size parameter"),

a is the sphere radius,

ϵ_1 is the permitivity of the infinite medium,

ϵ_2 is the real part of the permitivity of the sphere,

κ is the conductivity of the sphere, and

$\psi_l(\rho) = \rho j_l(\rho)$ (Ricatti-Bessel function).

The differential scattering cross section is defined as

$$\left. \frac{d\sigma}{d\Omega} \right|_\theta = \frac{dP_{scat}(\theta)/d\Omega}{\left| \vec{S}_{inc} \right|} \tag{17}$$

where

$$\frac{dP_{scat}(\theta)}{d\Omega} = r^2 \frac{c}{8\pi} \mathrm{Re}\left[\vec{E} \times \vec{H}^* \right]$$

$$= r^2 \frac{c}{8\pi} \mathrm{Re}\left[E_\theta H_\phi^* - E_\phi H_\theta^* \right] \hat{r} \tag{18}$$

(time averaged power scattered per unit solid angle into direction θ), and

$$\vec{S}_{inc} = n_1 \frac{c}{8\pi} \hat{z} \tag{19}$$

(time averaged incident flux).

The total scattering cross section is the integral of Eq. 18 over all solid angles. This is a very difficult task to perform, given the form of the scattered fields. It turns out that, for large r and for polarized incident wave, the total cross section (scattering plus absorption) can be determined from the differential scattering cross

36

section in the $\theta = 0$ direction [2]. That this is the case is due to conservation of energy. The total amount of radiation lost to scattering and absorption is just the amount of radiation left over propagating in the direction of the incident wave $(\theta = 0)$.

The total cross section, in the context of the current problem, is

$$\sigma = \sigma_{scat} + \sigma_{abs} = \frac{4\pi}{k_1}\text{Im}\left[\hat{x} \cdot \vec{E}(\hat{z})\right] \qquad (20)$$

where $\vec{E}(\hat{z})$ is the scattered electric field $(\vec{E}(\hat{z}))$ with the term $e^{ik_1 r}/r$ factored out, and evaluated in the direction of the propagation of the incident wave $(\hat{z})$. The dot product is then taken with the unit vector in the direction of the incident polarization $\hat{x}$. We note that $\vec{E}$ is easily extracted from Eqs. 13 and 14 because $\varsigma_l(k_1 r)$ and $\varsigma_l'(k_1 r)$ both go like $e^{ik_1 r}$ for large $k_1 r$ [2]. Equation 20 is known as the optical theorem.

By inserting Eqs. 13 and 14 into Eq. 20 the total cross section becomes [2]

$$\sigma = \frac{1}{k_1^2}\text{Re}\left[\sum_{l=1}^{\infty}(-i)^{l+1}l(l+1)\left(B_l^e + B_l^m\right)\right]. \qquad (21)$$

We also write here the differential scattering cross section for 180°, which we refer to as the backscatter cross section. We will use this in the next section. The backscatter cross section is determined by inserting Eqs. 13 and 14 into Eq. 18 and setting $\theta = \pi$:

$$\left(\frac{dP_{scat}}{d\Omega}\right)_{\theta=\pi} = -\frac{1}{k_1^2}\left|\sum_{l=1}^{\infty}\left[(B_l^e - B_l^m)\left(\frac{dP_l}{dx}\right)_{x=-1}\right]\right|^2, \qquad (22)$$

where P_l is the lth Legendre polynomial.

4.3   Computer Model

We have developed a computer program which calculates the total scattering cross section (Eq. 21) and the backscatter cross section (Eq. 22) for a dielectric, nonconductive sphere of arbitrary size. For zero conductivity $(\kappa = 0)$ there is no absorption and the total cross section is equal to the scattering cross section.

We use the results of this program to calculate the extinction coefficient and the backscatter coefficient for a collection of dielectric, nonconductive spheres. When

the spheres are randomly distributed and the spacing between spheres is large compared to the wavelength the extinction coefficient α and backscatter coefficient β are

$$\left\{ \begin{array}{c} \alpha \\ \beta \end{array} \right\} = \int_0^\infty N(a) \left\{ \begin{array}{c} \sigma \\ \left(\frac{dP}{d\Omega}\right)_\pi \end{array} \right\} da \qquad (23)$$

where $N(a)$, the size distribution, is the number of spheres, per unit volume, with radii between a and $a + da$. The normalization is $\int_0^\infty N(a)da = N_t$, where N_t is the total density of particles. The size distribution can be chosen arbitrarily.

All programs and subroutines were developed and run on an 80286 based computer. The infinite sums in Eqs. 21 and 22 were truncated at the first term which was less than some fraction of the accumulated sum of the previous terms. This was adequate for calculating cross sections for particles with radii up to approximately 50 times the wavelength.

4.4 Results and Conclusions

We first show results of calculations of total and backscatter cross sections for individual spheres. These results serve to verify that the program is working correctly. We then show results of calculations of extinction and backscatter coefficients for collections of spheres with size distributions typical of atmospheric aerosols.

4.4.1 Individual Spheres

Figure 15 shows the total and backscatter cross section *efficiencies* for a single sphere versus size parameter. The cross section efficiency (total or backscatter) is the cross section divided by the cross sectional area πa^2 of the sphere, where a is the particle radius. The size parameter is $2\pi a/\lambda_1 = k_1 a$. The indices of refraction for these plots are $n_1 = 1$ (surrounding medium: vacuum) and $n_2 = 1.33$ (sphere: water).

We note several observations from these plots which serve to verify the proper operation of the program:

- For small size paramater both cross section efficiencies go as the particle size parameter raised to the fourth power. For small size parameter we expect the

Mie Scattering cross section efficiencies
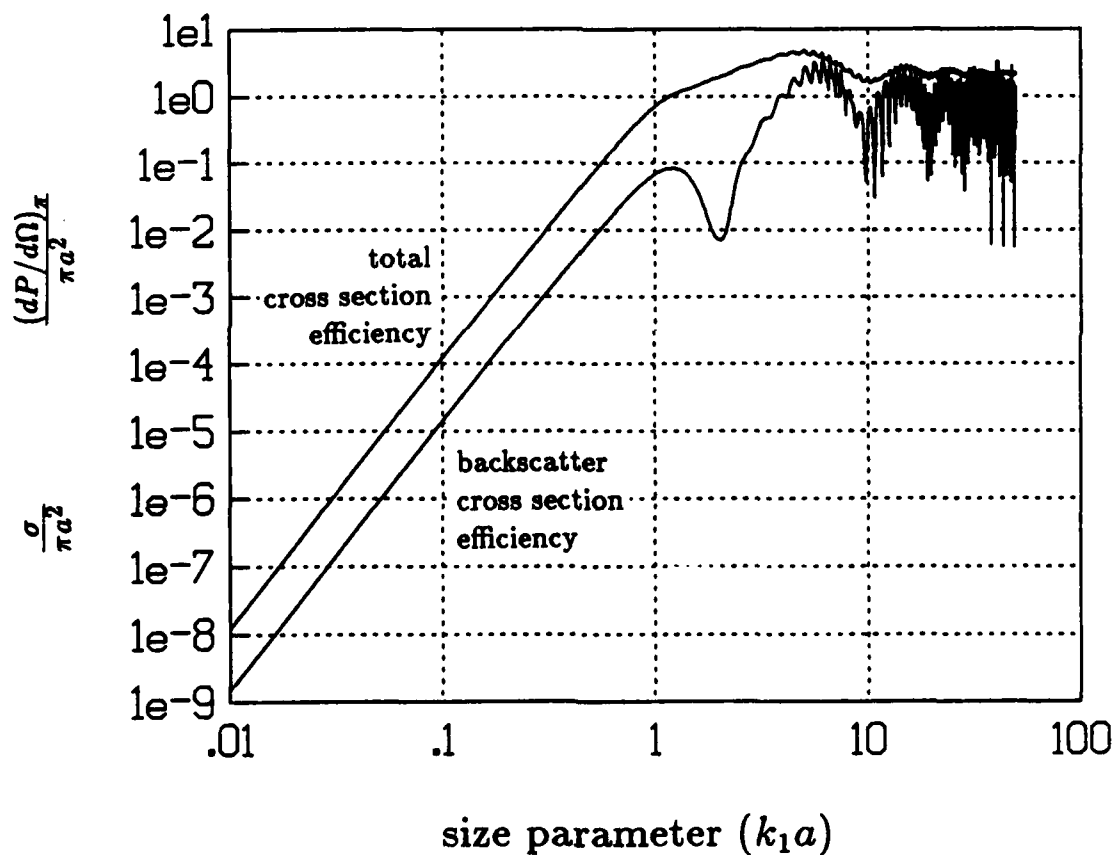$$n_1 = 1.0 \quad n_2 = 1.33$$

Figure 15: Mie total and backscatter cross section efficiencies versus size parameter for $n_1 = 1$, $n_2 = 1.33$, and $\kappa = 0$.

Mie scattering solution to reduce to Rayleigh scattering solution. In Rayleigh scattering the cross section goes as (particle volume)$^2/\lambda^4$, or as r^6/λ^4. Therefore, cross section efficiency goes as r^4/λ^4, which we observe.

- The ratio of backscatter cross section efficiency to total cross section efficiency to is 0.12 for small size parameters. For Rayleigh scattering this ratio is $3/8\pi \approx 0.12$.

- The total cross section efficiency approaches the value 2 for large size parameters. For large size parameters, we expect the Mie scattering solution to reduce to the result obtained from scalar diffraction theory. For an arbitrary shaped obstacle which is large compared to the wavelength and does not transmit much light the main contribution to the forward scattered light is from Fraunhofer diffraction. For distances far from the obstacle this total cross section is $2D$, where D is the cross sectional area of the obstacle as "seen" by the incident plane wave. The efficiency is therefore 2.

Note the very fast fluctuations in both cross sections as a function of size parameter for size parameters greater than approximately one. (Because of the log scale the fast fluctuations in total cross section efficiency appear small.) This is the result of adding coherently all the partial waves of each subfield (each term of the sums in Eqs. 21 and 22). The ratio of backscatter cross section to total cross section in this regime is very complicated and would not be very useful experimentally. Fortunately, a size distribution with a variance large compared to these fluctuations tends to average out the fluctuations. This, as we show below, is what happens for atmospheric aerosol scattering.

4.4.2 Collection of Spheres

There are many different size distributions which describe the many different types of particles of the lower troposphere. We have not performed a study of particle sizes in the atmosphere. Our intention here is to consider size distributions generally accepted as describing some atmospheric constituents and to use them with the Mie formulation to determine the behavior of the ratio of backscatter coefficient to total

extinction coefficient. We present two size distributions below.

A size distribution used to describe the fine water aerosols which form so-called continental haze [4] is

$$N(a) = \frac{J}{a^{\nu_p+1}} \qquad (24)$$

where ν_p is a constant which is usually between 2.0 and 5.0 and J is a normalization constant. This power law model was originally propose by Junge [5].

A size distribtion that is found to represent clouds and fogs [4] takes the form

$$N(a) = C \left(\frac{a}{a_m}\right)^{\nu_p} e^{-a/a_m} \qquad (25)$$

where a_m, the mode radius, is the value of a for which $N(a)$ is maximum and C is the normalization constant. ν_p determines the spread of the distribution about the maximum. This model has been discussed in detail by Deirmendjian [6,7].

Figure 16 shows a plot of backscatter efficiency versus extinction efficiency for the haze model. Each point represents a calculation of Equation 23 with a different value of ν_p in the continental haze size distribution. The values of ν_p are in the range of 2–5 in steps of 0.05. The single particle Mie scattering formulation with conditions identical to those of Fig. 15 are used.

Figure 17 shows four plots of backscatter efficiency versus extinction efficiency for the cloud/fog model. Each plot corresponds to a different value of ν_p, as marked. Each point in each plot represents a calculation of Equation 23 with a different value of $k_1 a_m$ in the fog/cloud size distribution. The values of $k_1 a_m$ are in the range of 0.1–50. The step is 0.1 in the range 0.1–1 and 1 in the range 1–50. Again, the single particle Mie scattering formulation with conditions identical to those of Fig. 15 are used.

The plot in Fig. 16 indicates that the assumption of constant backscatter to extinction ratio for the continental haze model is fairly good. The plots of Fig. 17 indicate that the assumption for the cloud/fog model is fairly good for mode radius larger than a certain amount, dependent of ν_p. For large mode radius the integral in Eq. 23 has largest contributions from the scalar diffraction regime of Mie scattering. For small mode radius the assumption is not as good, but still not too bad. Here the integral has large contributions from the intermediate regime between Rayleigh scattering and scalar diffraction.

41

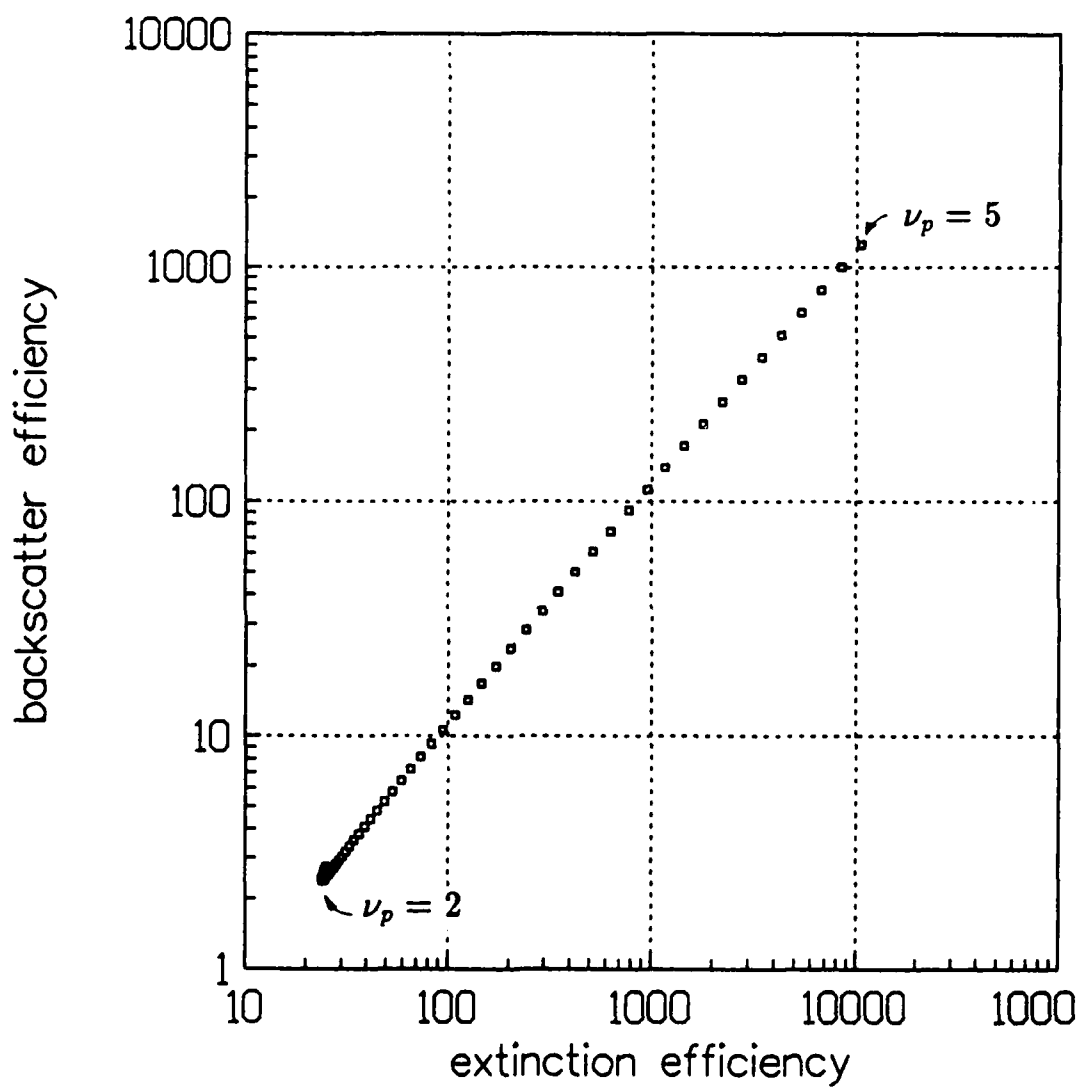Figure 16: Backscatter versus extinction efficiencies for different values of ν_p of the continental haze model.
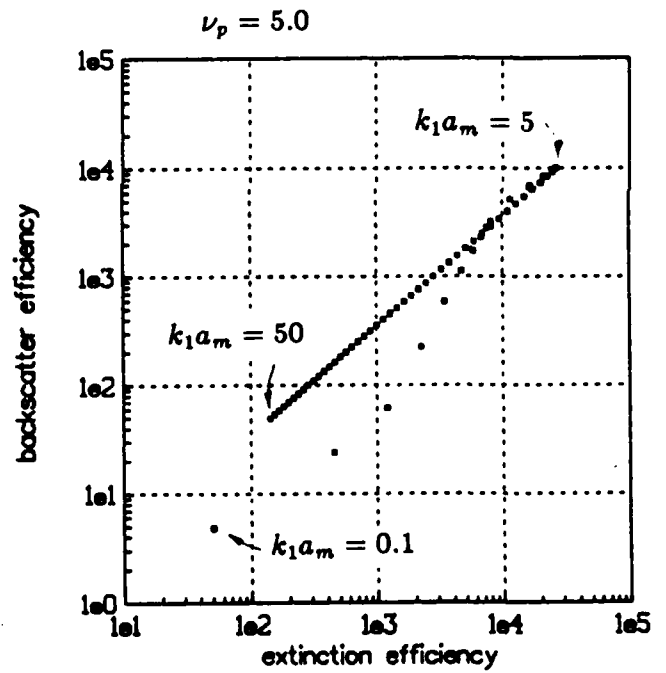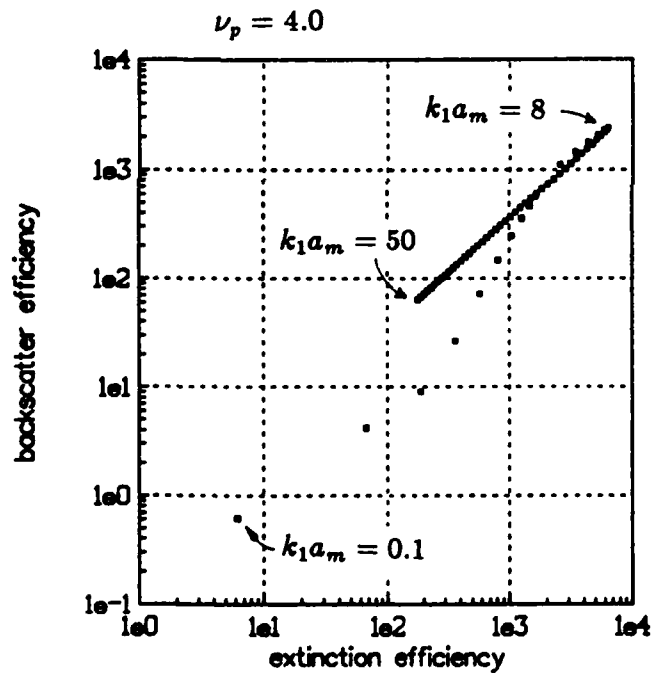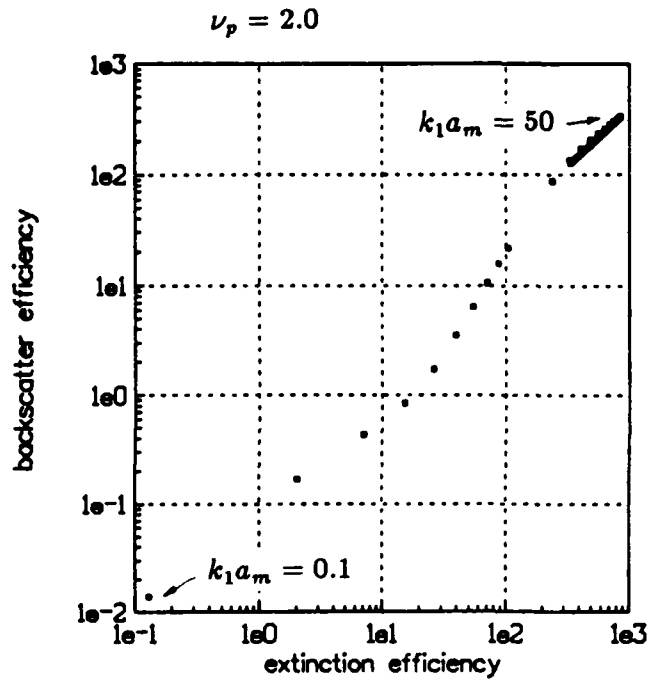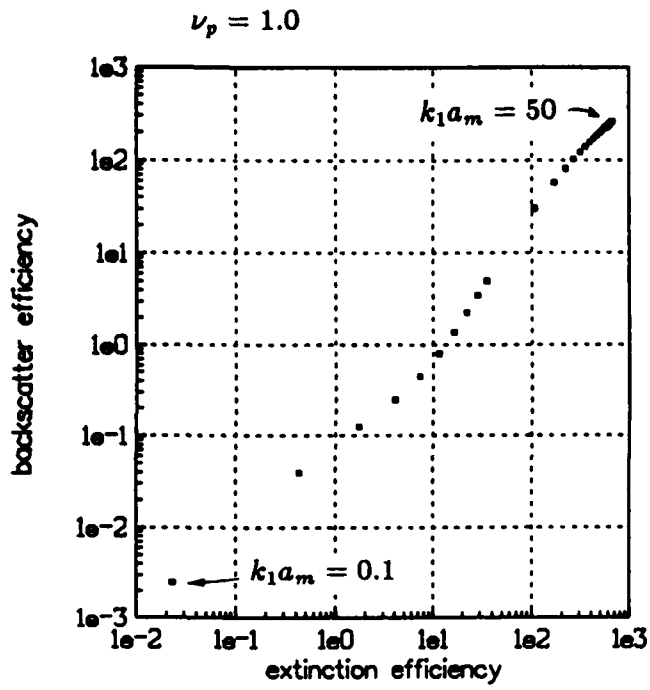
Figure 17: Backscatter versus extinction coefficients for different values of ν_p and mode radius a_m of the cloud/fog model.

5 Extinction

5.1 Introduction

A major use of the low altitude lidar system is in determining the extinction coefficient for a variety of meterological conditions in the troposphere. The extinction coefficient is determined from lidar data only with the aid of assumptions, models, or additional experiments which are independent of the lidar data. Our work has involved testing the validity of the extinction calculations, understanding their limitations, and enhancing the extinction algorithm.

Section 5.2 describes the standard Klett inversion method that is the basis of all of our extinction calculations. It describes the inversion algorithm (Section5.2.1), our methods of determining the extinction at the final range of interest (Section 5.2.2), and some calculations with artificial data (Section 5.2.3). Section 5.3 shows the results of extinction calculations made in clear air and clouds (Section 5.3.1) and falling snow (Section 5.3.2). The results for falling snow were used for the polarization studies described in Section 3.4.

5.2 Theoretical Background

5.2.1 Inversion

The range resolved extinction coefficient $\alpha(r)$ is determined from the lidar data with the Klett inversion method. The Klett inversion [8] is a (numerically) stable solution to the single scatter lidar equation. It requires knowledge of the extinction coefficient at the final range value of interest.

The single scatter lidar equation is

$$P(r) = P_o \frac{c\tau}{2} A \frac{\beta(r)}{r^2} \exp\left[-2 \int_0^r \alpha(r')dr'\right] \qquad (26)$$

where $P(r)$ is the instantaneous range resolved received power, P_o is the transmitted power, c the velocity of light, τ the pulse duration, and A the effective receiver area. $\beta(r)$ is the backscatter coefficient ($\mathrm{km}^{-1}\mathrm{sr}^{-1}$) and $\alpha(r)$ is the extinction coefficient (km^{-1}), both at a range r from the receiver/transmitter.

Equation 26 has two unknowns: $\alpha(r)$ and $\beta(r)$. To solve Eq. 26 we assume the relationship $\beta = C\alpha^k$, where C and k are constants. We have addressed the validity

of this relationship in Section 4.4. The lidar equation is then rewritten as

$$\frac{dS}{dr} = \frac{k}{\alpha}\frac{d\alpha}{dr} - 2\alpha \tag{27}$$

where $S = \ln\left[r^2 P(r)\right]$ is called the log squared corrected power.

Equation 27 is a form of Ricatti equation which is exactly soluble. Since it is a first order differential equation, the solution is specified with one arbitrary initial condition. It is typical to choose the initial condition as the value of the independent variable (α in this case) at the beginning of the range interval for which solution is desired. However, doing so in this situation leads to a numerically unstable solution.

The numerically stable solution put forth by Klett involves choosing the "initial" condition at the end of the range interval. The solution is

$$\alpha(r) = \frac{\exp\left(\frac{S-S_f}{k}\right)}{\frac{1}{\alpha_f} + \frac{2}{k}\int_r^{r_f} \exp\left(\frac{S-S_f}{k}\right)\,dr'} \tag{28}$$

where $S_f = S(r_f)$, $\alpha_f = \alpha(r_f)$, and r_f is the final range of interest. Equation 28 is used for $r < r_f$. Equation 28 is the solution we use for determining extinction coefficients from lidar data.

The Klett inversion of lidar data can be performed on-line with the the lidar control program. The details of the implementation are described in Part II. The program will allow a value for α_f to be specified, or it will choose on the basis of the one of the algorithms described in the next section.

5.2.2   Initial Condition

From a mathematical point of view the initial condition α_f is arbitrary. Therefore, the only correct way of specifying α is by measuring it. However, there are ways of making "smart" guesses. Below we describe two methods which we have implemented in the lidar control program. The first method, which assumes α to be constant in a small interval near r_f, is standard and used throughout the lidar community. The second method, which assumes α to be a linear function of r near r_f, is an enhancement that we developed.

Constant α_f

45

This method assumes that α is a constant function of range near r_f. The lidar equation (Eq. 27) for constant α has the solution

$$\alpha = -\frac{1}{2}\frac{dS}{dr}.$$ (29)

Therefore, if α is constant then the slope of S must be constant. The "best" α_f can therefore be found by determining the linear least squares slope of S for the some number of data points near the final range for which a solution is desired.

For a positive slope of S this method breaks down because it would result in a negative extinction coefficient. The reason is that the assumption of constant α is no longer valid. This might happen when the extinction coefficient increases very quickly, as is the case at the interface between clear air and a cloud. The second method of choosing α_f does not suffer from this problem.

Linear α_f

This method assumes that α is an arbitrary linear function of range (not necessarily constant) near r_f. If we write

$$\alpha = Ar + B,$$ (30)

where A and B are unknown constant parameters to be determined, then the lidar equation (Eq. 27) becomes

$$\frac{dS}{dr} = \frac{kA}{Ar + B} - 2(Ar + B).$$ (31)

The "best" A and B are found by least square fitting the data near r_f to Eq. 31. That is, the best A and B are those that minimize the function

$$I(A, B) = \sum_{i=n-m}^{n}\left[\frac{dS_i}{dr} - \left(\frac{kA}{Ar_i + B} - 2(Ar_i + B)\right)\right]^2$$ (32)

where r_i is the range corresponding to the ith data point, $S_i = S(r_i)$, $r_n = r_f$, and m is one less than the number of data points considered near r_f for the least squares fit.

Minima of the function $I(A, B)$ with respect to A and B would typically be found by solving

$$\frac{\partial I}{\partial A} = 0$$
$$\frac{\partial I}{\partial B} = 0.$$ (33)

46

However, this nonlinear system of equations cannot be solved analytically and we therefore resort to a numerical technique to minimize I.

A simplex method [9] is used to minimize I with respect to A and B. Initially, three points are chosen in the $A - B$ plane. One of these points can be $A = 0$ and B equal to the α_f found from the first method of determining α_f ("constant α_f" method, described above). The other two points are near the first point. Next, of these three points the point which gives maximum I is reflected across the line connecting the other two points. The value of I at this new point will be less than the values at the other points (for well-behaved I). This process is continued until the percent change of the value of I at the new point, relative to the previous point, is less than some desired tolerance.

5.2.3 Extinction Calculations with Artificial Data

We have tested the extinction algorithm with artificially created data. Assuming an extinction profile shown by the solid line in Fig. 18b we calculate the lidar power which would give this profile (Fig. 18a. We then calculate the extinction coefficient with the Klett algorithm. The data shown in Fig. 18a could be an idealization of a lidar return from a cloud.

The nonsolid lines in Fig. 18 show the calculated extinction for different choices of α_f. The final range r_f is chosen past the cloud. Two of the α_f values are chosen by the two methods described in the previous section (constant and linear α_f methods. The calculated extinctions for these two values of α_f lie almost entirely on the model extinction curve and are difficult to see. Both values of α_f for the two methods are almost the same.

The other values of α_f are chosen to illustrate the stability of the inversion algorithm. Note that values of α_f quite different from the true α_f give solutions that quickly converge to the true solution.

Figures 19 and 20 are similar to Fig. 18 except that random Gaussian noise is added to the artificially created lidar return before calculating the extinction coefficient. The standard deviation of the Gaussian noise of Figure 20 is ten times that of Fig. 19. In both figures the extinction calculation is initiated in the cloud,
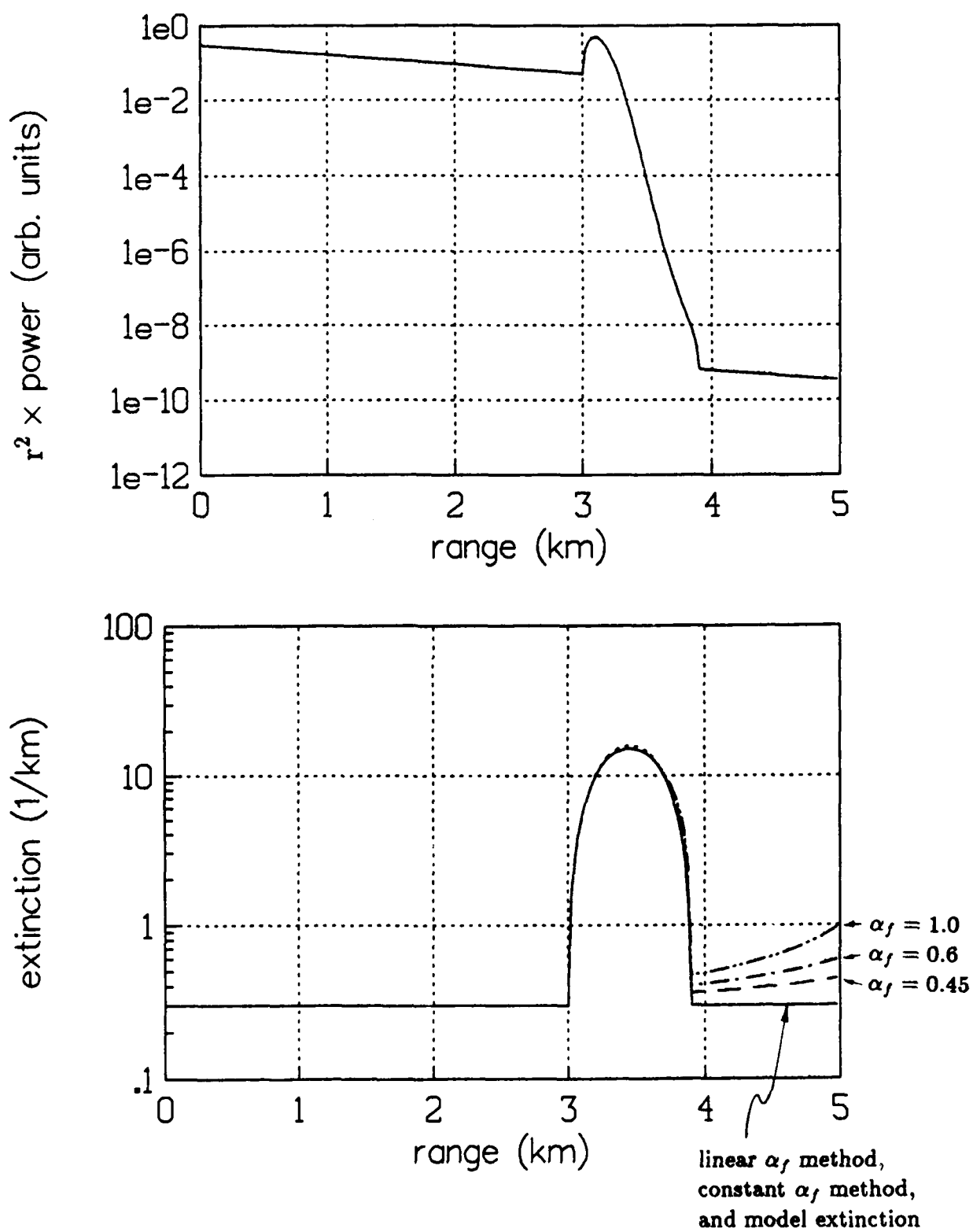
Figure 18: a) Artificial lidar return. b) Solid line: model extinction profile. Others: Klett inversions with different α_f's.

since the data after the cloud is too noisy. Both figures show calculations with the linear and constant α_f methods. The linear α_f calculation is initiated in a region where the constant α_f method could not be used because $dS/dr > 0$.

5.3 Extinction Calculations with Real Data

5.3.1 Clear Air and Clouds

Figure 21 shows a lidar return from clear air along with a Klett inversion. A value of α_f was chosen by assuming α to be constant over the final ten range points considered.

Figure 22 shows a lidar return with a cloud, and a Klett inversion through the cloud. A value of α_f was chosen by assuming α to be constant over the final four range points considered.

The lidar returns in these two figures were acquired during daytime in Sudbury, MA. We find that the extinction coefficient during clear air conditions there to be in the range of 0.1 to 0.5 km^{-1}. The extinction coefficient in the cloud of Fig. 22 indicates that the laser power was too low to observe the top side of the cloud.

5.3.2 Falling Snow

We find that the the technique of calculating the extinction coefficient from lidar is quite robust. This is revealed by our calculations using data from falling snow. In our polarization studies of Section 3.4 we presented and used the lidar calculated extinction coefficients in several plots. Here we show the validity of this by comparing these extinction calculations with data from other groundbased instruments.

During acquisition of lidar data in falling snow on Feb. 4, 1988 data was simultaneously acquired with a Particle Measurement Systems (PMS) rain distrometer and a visibility meter. Both instruments were located on the ground approximately four meters from the lidar transmitter/receiver. The visibility meter measures the extinction coefficient directly. It acquires data at a ten second rate.

The rain distrometer measures the snow fall rate ($cm^{-2}sec^{-1}$) and the distribution of snowflake diameters in one dimension (snowflakes interrupt a laser beam and cast a shadow on a 64 pixel line detector). We assume that each snowflake is

Figure 19: a) Artificial lidar return with Gaussian noise. b) Dotted line: model extinction. Solid lines: calculated extinctions.
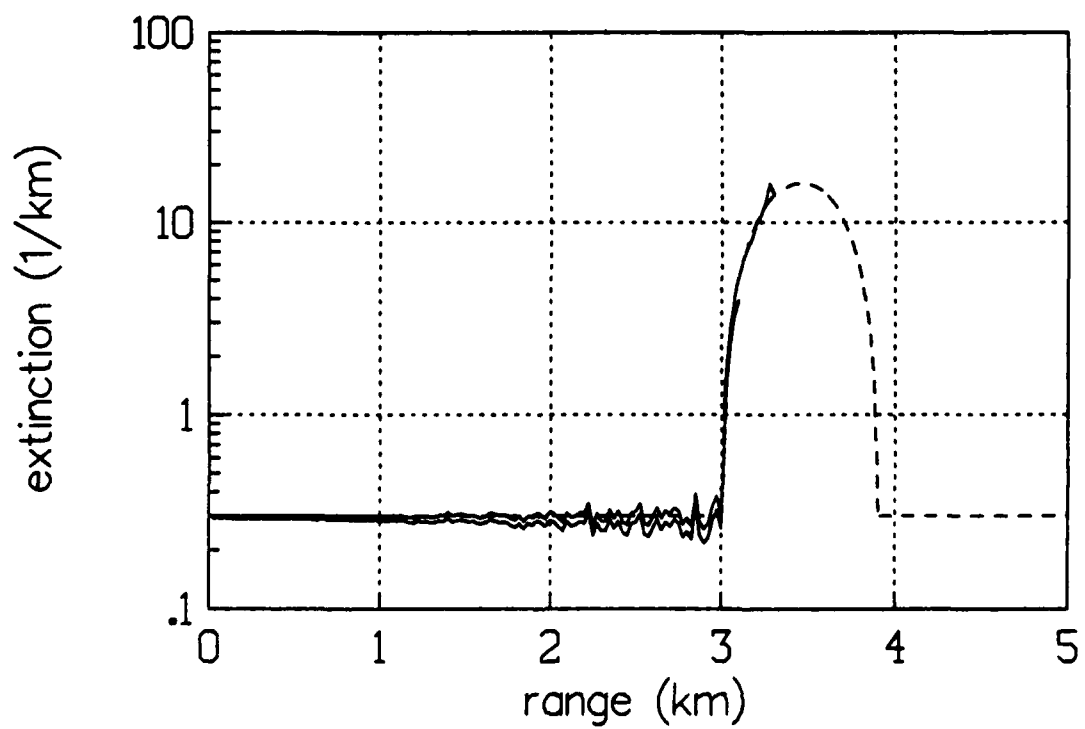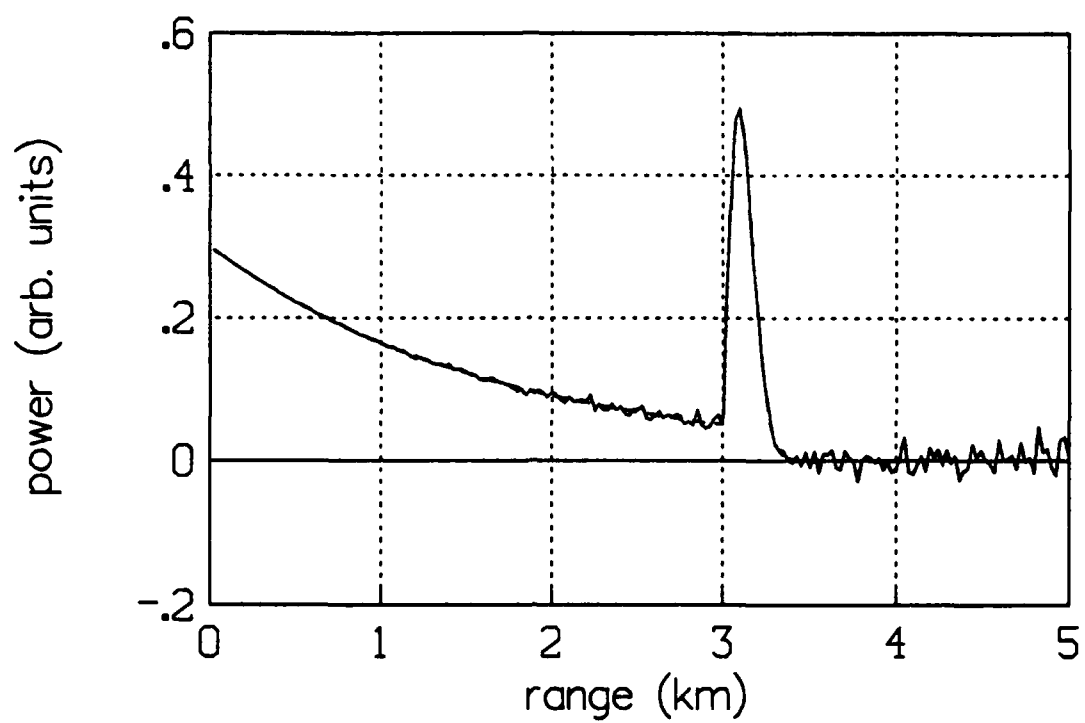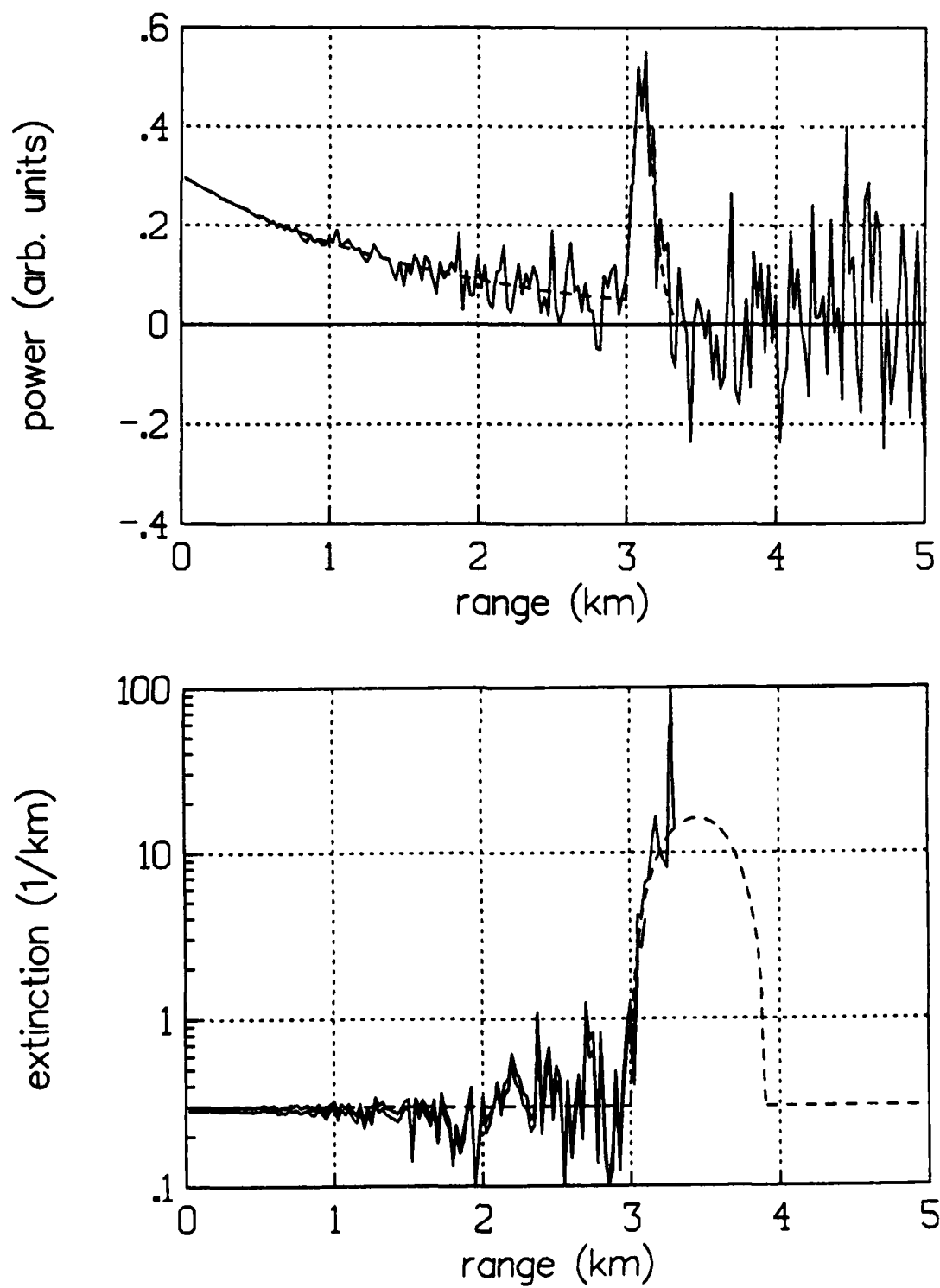
Figure 20: a) Artificial lidar return with Gaussian noise. b) Dotted line: model extinction. Solid lines: calculated extinctions.
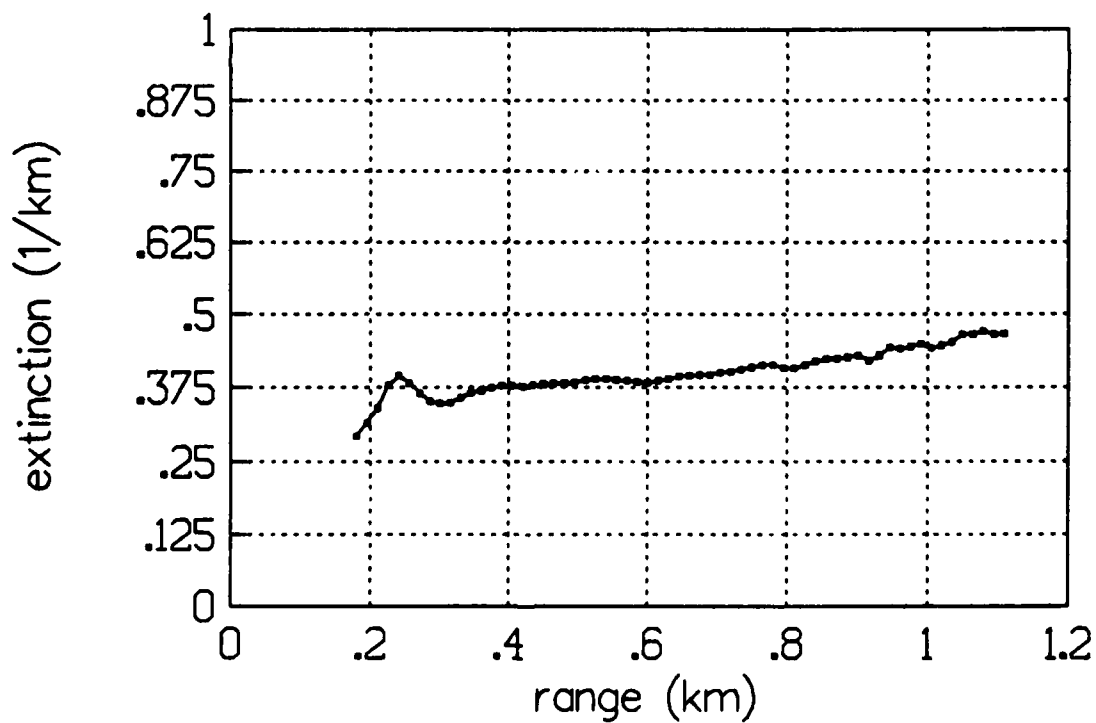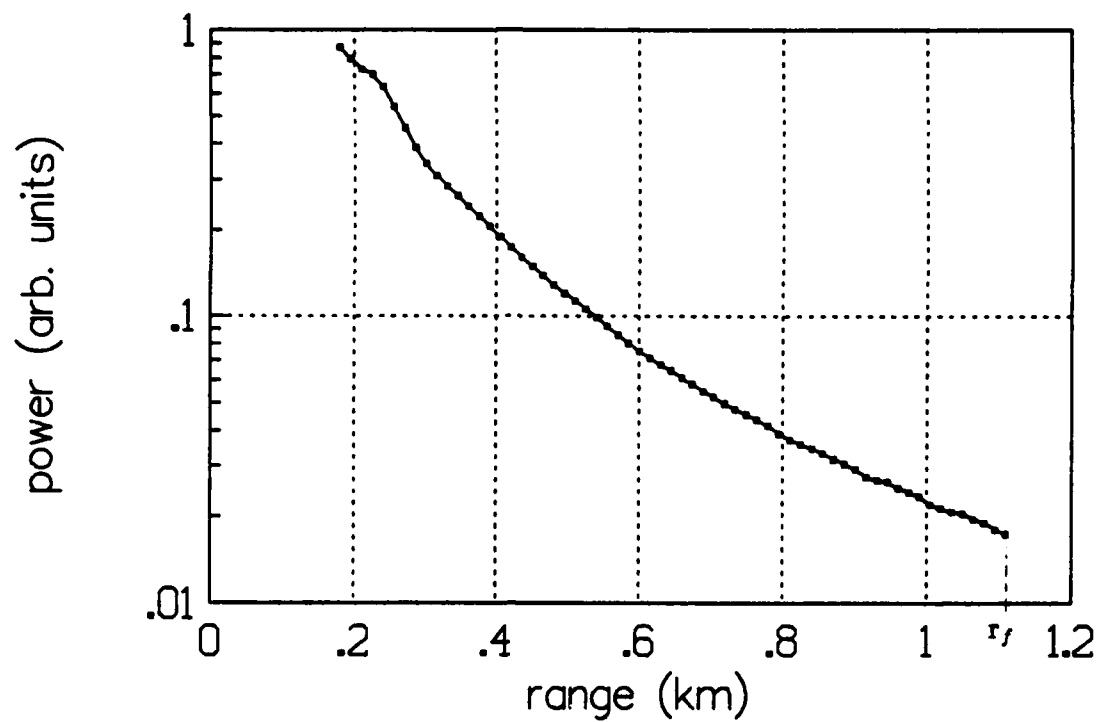
Figure 21: a) Lidar return from clear air and b) a corresponding Klett inversion.
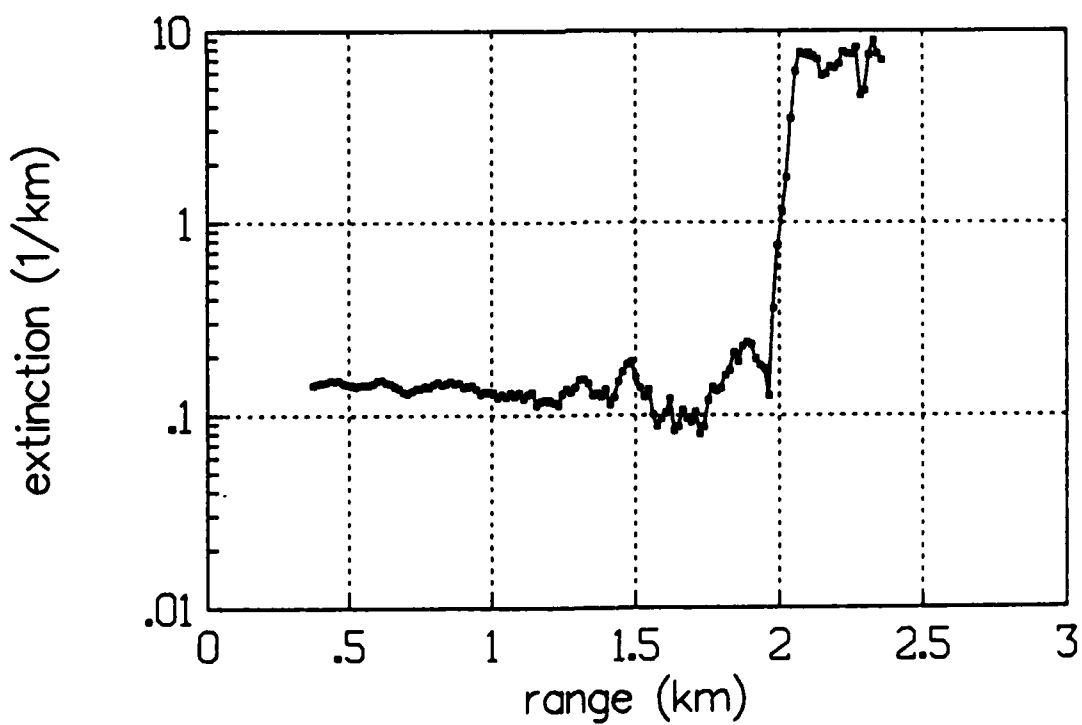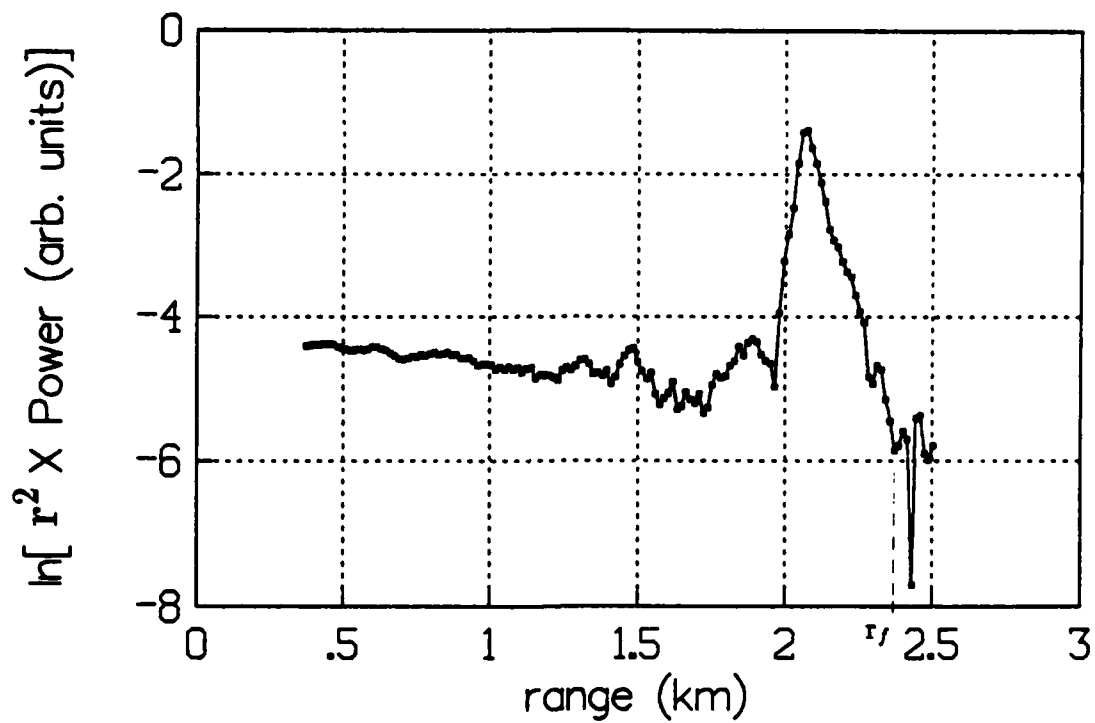
Figure 22: a) Lidar return from a cumulus cloud and b) a corresponding Klett inversion.

circular with the measured diameter. Then, the density of particles N_i with radii a_i ($i = 1, \ldots, 64$; a_i are the measured diameters divided by two) is determined by multiplying by the snow fall velocity, which we asuume to be 50 cm/sec [10] for all snowflakes. The total density N_t is then

$$N_t = \sum_{i=1}^{64} N_i \Delta a, \tag{34}$$

where Δa is the distance between pixels.

The extinction coefficient α is determined by assuming an extinction efficiency of 2 (which is the case for particles large compared to a wavelength—see Section 4). Then,

$$\alpha = 2 \sum_{i=1}^{64} \pi a_i^2 N_i \Delta a. \tag{35}$$

Figure 23 shows the extinction coefficient determined with the visibility meter versus lidar calculated extinction coefficient. Figure 24 shows extinction coefficient determined with the rain distrometer versus lidar calculated extinction. Each point in each graph corresponds to a particular lidar return. The lidar extinction shown is the average extinction, calculated with the Klett inversion, over the interval 180–500 m. Visibility and rain distrometer data for each point corresponds to an average over a four minute interval starting at the time of the lidar return.

Also shown in Figs. 23 and 24 are the correlation coefficients and the least squares slopes between the visibility meter and lidar and between the rain distrometer and lidar respectively. The correlations are 0.95 and 0.82 in the first and second plots respectively. These are fairly high correlations and we feel that this indicates that the lidar is a useful tool for determining extinction in snow.

There are seveal reasons why the correlations are not unity. The lidar measures a spatially averaged extinction coefficient, averaged over a relatively short time interval. The visibility meter and rain distrometer measure a temporally averaged extinction coefficient, averaged over a relatively small region of space. Furthermore, the regions of space do not overlap.

The lidar extinction calculation uses the assumption of constant ratio between backscatter and extinction coefficients along the entire propagation path. We expect this to be true for snow only on average. Because of the random shape and orien-
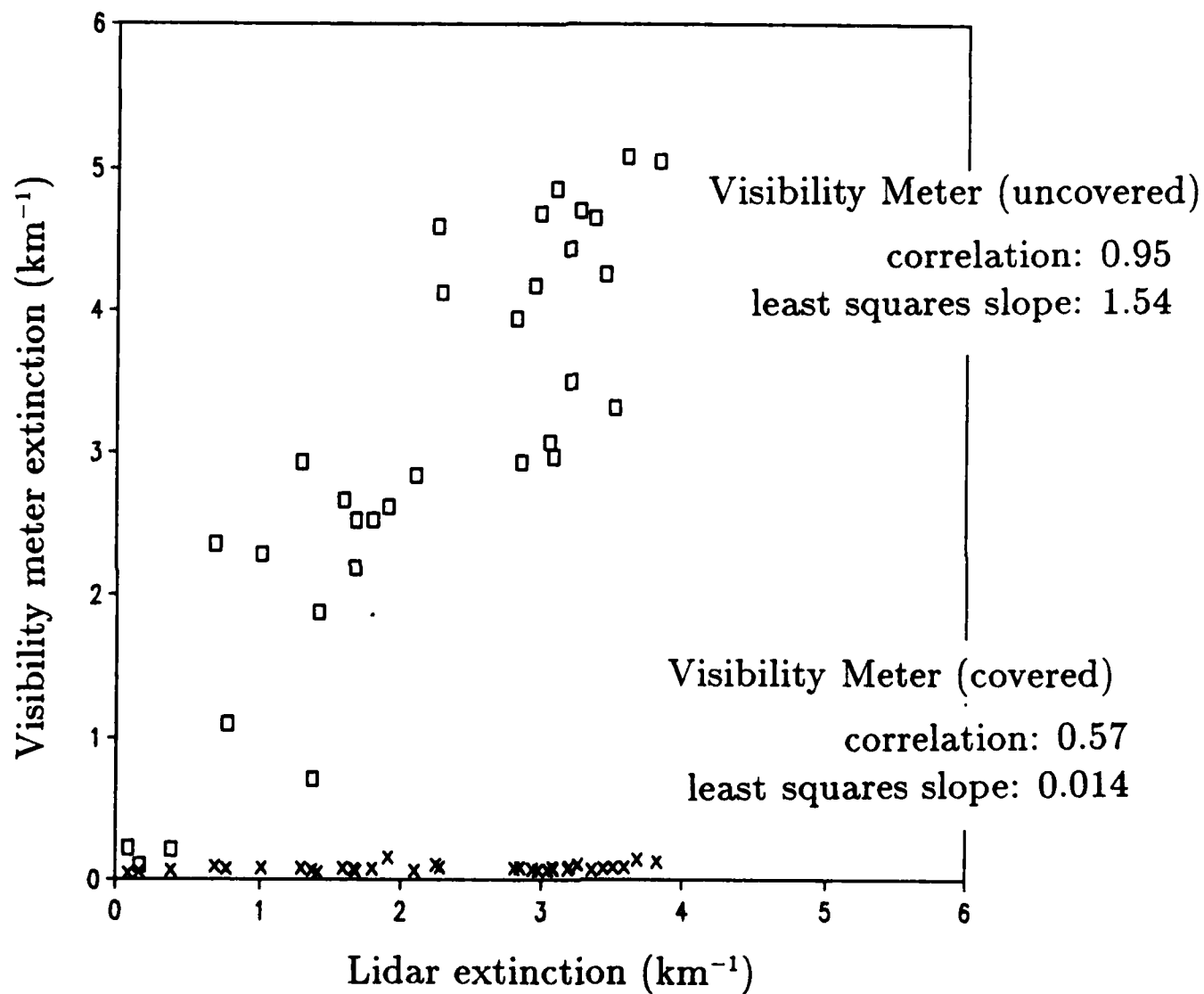
Figure 23: Visibility meter extinction coefficient versus lidar extinction coefficient.
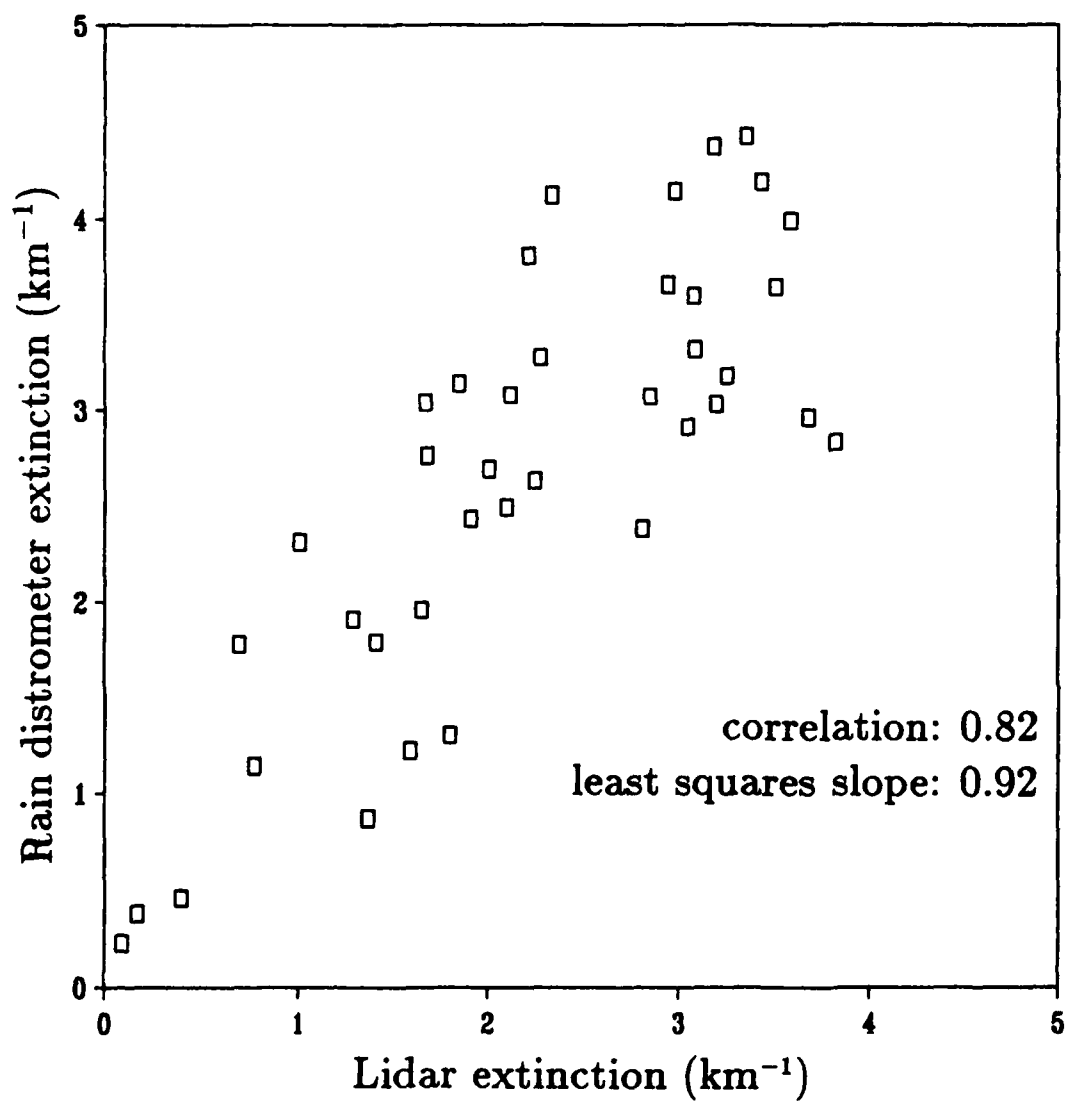
Figure 24: Rain distrometer extinction coefficient versus lidar extinction coefficient.

tation of snow, this ratio might fluctuate about some average value, much like the degree of polarization of the backscattered radiation, as we discussed in Section 3.4.

6   Multiple Scattering

6.1   Introduction

PhotoMetrics has done some preliminary modeling of multiple scattering effects for lidar. Although we do not have results from this work yet, we have defined a direction along which these modeling efforts could be pursued. We have determined a theoretical approach and have derived expressions for the backscattered power based on this appoach.

Section 6.2 briefly discusses the theoretical background. It identifies the different theoretical approaches which are used in multiple scattering theory.

Section 6.3 discusses the radiative transfer equation, the approach that we have chosen to take.

Section 6.4 describes our application of the radiative transfer equation to a particular lidar problem.

6.2   Background

Multiple scattering increases in significance as optical path length increases. For lidar it is important to consider multiple scattering after a few hundred meters in cumulus clouds, a few kilometers in moderate snow, and greater than approximately ten kilometers in clear urban aerosols.

Many techniques exist which include multiple scattering effects in calculating light propagation in a random distribution of scatterers such as the atmosphere. These techniques are either analytical or Monte Carlo. The analytical techniques are either transport theory or multiple scattering theory.[4] Monte Carlo techniques are applied to either of these analytical techniques.

Transport theory, which treats the medium as a continuum, uses the radiative transfer equation for the specific intensity. The radiative transfer equation is similar to the Boltzmann equation for the phase space distribution function of particles in

---

[4]This terminology is from Ishimaru [11].

a gas or plasma. The Boltzmann equation for gases is typically a seven dimensional problem: three spatial dimensions, three momentum or velocity dimensions, and time. The radiative transfer equation is a six dimensional problem for each of the four polarization degrees of freedom: three spatial dimensions, two direction dimensions, and time.[5] Thus, the radiative transfer equation may have as many as 24 degrees of freedom.

Multiple scattering theory treats the medium as a collection of discrete scatterers. It starts with Maxwell's equations, or a reduced form of Maxwell's equations such as the scalar wave equation, obtains a solution for single particle scattering, and then introduces the interaction for many particles. This is typically done by summing over all possible single scatters that can occur. Solutions are typically of the form of statistical averages and correlations of field quantities.

We have decided to formulate the multiple scattering problem using the radiative transfer equation.

6.3 Radiative Transfer Equation

The time dependent radiative transfer equation is four coupled integro–differential equations in the four Stokes parameters. We will only consider the radiative transfer equation for the specific intensity, the first Stokes parameter. Therefore, we are neglecting changes in the polarization of the radiation due to multiple scattering.

The time dependent radiative transfer equation is then

$$\frac{\partial I(\vec{r}, \hat{s}, t)}{\partial t} + \hat{s} \cdot \nabla_r I(\vec{r}, \hat{s}, t) + \alpha_t I(\vec{r}, \hat{s}, t) = \frac{\alpha_t}{4\pi} \int_{4\pi} p(\hat{s}, \hat{s}') I(\vec{r}, \hat{s}', t) d\Omega' \qquad (36)$$

where $I(\vec{r}, \hat{s}, t)$ is the specific intensity (W/m^2–sr–sec–Hz) at position $\vec{r}$ propagating in direction $\hat{s}$ at time t, α_t is the total extinction cross section (total cross section times particle density), α_s is the extinction cross section due to scattering (scattering cross section times particle density), and $p(\hat{s}, \hat{s}')$ is the scattering phase function from direction $\hat{s}$ to $\hat{s}'$. The phase function is normalized such that

$$\frac{1}{4\pi} \int_{4\pi} p(\hat{s}, \hat{s}') d\Omega' = \frac{\sigma_s}{\sigma_t} \equiv W_o. \qquad (37)$$

---

[5]The direction in the radiative transfer equation is equivalent to velocity in the Boltzmann equation. However, two directions completely specify the third direction since the magnitude is the speed of light.

W_o is called the single particle albedo. Equation 36 assumes no sources of radiation other than those specified by boundary conditions (e.g., there is no blackbody radiation emitted at every point in space).

For lidar it is usually possible to reduce the number of degrees of freedom of Eq. 36 to achieve a tractable problem. For example, for spherical particles and cylindrically symmetric incident laser radiation, the specific intensity is independent of azimuth angle. For isotropic scattering the specific intensity is independent of the angular direction orthogonal to the laser propagation direction. For large particles, from which scattering is primarily in the forward direction, the time variable can be eliminated (time would be equivalent to distance along the direction of laser propagation). For optically thick media in which large numbers of multiple scatters occur, the radiative transfer equation reduces to a diffusion equation.

6.4 Preliminary Modeling

We have done preliminary modeling of the multiple scattering problem by applying the radiative transfer equation to an urban aerosol atmosphere, a medium often encountered in our lidar work. For such a medium the extinction coefficient is typically on the order of 0.1 km^{-1}. Therefore, for lidar paths less than 10 km, more than two to three scatters is unlikely. Furthermore, the particles are large compared to the wavelength of light. Therefore, as is borne out by Mie scattering theory, scattering is concentrated in a small cone about the forward direction.

For this application we can assume that the transmitted wave propagates in the forward direction, attenuating along the way by scattering and absorption, undergoes one backscatter, and propagates back to the receiver, again attenuating along the way by scattering and absorption. Light can scatter in and out of the main propagation path many times, but only by small angles.

For this application it is valid to neglect changes in polarization. Most scatters are small angle, except for the one backscatter, which most likely preserves polarization. Therefore we may use Eq. 36 (only total specific intensity need be considered).

Eq. 36 can be reduced from a 6 dimensional problem to a 3 dimensional problem. Time is eliminated as a degree of freedom; since the scattering angles are small

distance from the transmitter is equivalent to time.

There is azimuthal symmetry in space $\vec{r}$ and in direction $\hat{s}$. The density of the medium is assumed homogeneous and the incident radiation is assumed azimuthally symmetric. The particles are assumed to have an azimuthally symmetric scattering phase function.

A "solution" of the radiative transfer equation, for large particles, is given by Ishimaru [11]. The solution is written as the following Fourier integral

$$I(z,\vec{\rho},\hat{s}) = \frac{1}{(4\pi)^4} \int d\vec{\kappa} e^{-i\vec{\kappa}\cdot\vec{\rho}} \int d\vec{q} e^{-i\hat{s}\cdot\vec{q}} \left[F_0(\vec{\kappa},\vec{q}+\vec{\kappa}z)K(z,\vec{\kappa},\vec{q})\right], \qquad (38)$$

where

$$F_0(\vec{\kappa},\vec{q}) = \int d\vec{\rho} e^{i\vec{\kappa}\cdot\vec{\rho}} \int d\hat{s} e^{i\hat{s}\cdot\vec{q}} I(0,\vec{\rho},\hat{s}) \qquad (39)$$

$$K(z,\vec{\kappa},\vec{q}) = \exp\left[-\int_0^z \alpha(z')\left(1 - \frac{1}{4\pi}P(\vec{q}+\vec{\kappa}(z-z'))\right)dz'\right] \qquad (40)$$

$$P(\vec{q}) = \int d\hat{s} e^{i\hat{s}\cdot\vec{q}} p(\hat{s}). \qquad (41)$$

In these expressions $\vec{\rho} = x\hat{x} + y\hat{y}$, $\vec{\kappa}$ is the Fourier transform variable corresponding to the variable $\vec{\rho}$, and $\vec{q}$ is the Fourier transform variable corresponding to the variable $\hat{s}$.

Equation 38 indicates that, in Fourier transform space, the function K "propagates" the initial condition F_0 (the Fourier transform of the initial flux) to the final solution. K is referred to as the propagator. Here the propagator is a function of the Fourier transform P of the scattering phase function p.

In adopting this solution to our problem we use Eq. 38 to propagate the incident radiation at $z = 0$ to a height $z = z_h$. The result is multiplied by a number (the backscatter coefficient). This result is then used as the initial specific intensity for propagation back down to $z = 0$. By multiplying the solution at z_h by the backscatter coefficient (instead of integrating over solid angles) we assume the radiation to specularly reflect with reflectivity given by the chosen backscatter coefficient.

Additional assumptions are

- The initial specific intensity is that of a Gaussian beam:

$$I(0,\vec{\rho},\hat{s}) = \frac{k^2\rho_T^2 I_0}{\pi} \exp\left(-\frac{\rho^2}{\rho_T^2} - \frac{s^2}{\theta_T^2}\right), \qquad (42)$$

where ρ_T is the beam radius and $\theta_T = \eta/k\rho_T$ is η times the diffraction limited transmitter beam spread $(1/k\rho_T)$. η is a free parameter.

- The scattering phase function is (Ishimaru [11] uses this phase function)

$$p(\hat{s}) = 4\alpha_p W_0 e^{-\alpha_p s^2} \tag{43}$$

where $W_0 = \sigma_s/\sigma_t$ is the single particle albedo and α_p gives the angular spread of the single scattered cone of radiation. α_p is proportional to $(D/\lambda)^2$, where D is the diameter of the particle.

- The area function for the receiver is

$$A(\vec{\rho}, \hat{s}) = \begin{cases} A_r, & \rho <= \rho_R \\ 0, & \rho > \rho_R \end{cases} \tag{44}$$

where A_r is the physical area of the receiver aperture and ρ_R is the aperture radius. The power collected by the receiver is the integral of: (the specific intensity at the receiver multiplied by the area function).

The solution to our problem is the power $P(z_h)$ collected by the receiver due to scattering at height $z = z_h$. Normalized to the incident power P_T the solution is the following three dimensional integral:

$$\frac{\Gamma(z_h)}{P_T} = \beta(z_h)e^{-2\int_0^{z_h} \alpha(z)dz} \int_0^{2\pi\sqrt{2}} d\Delta \int_0^\infty d\kappa \int_0^\infty dq(2\pi\sqrt{2} - \Delta)f(\kappa, q, \Delta), \tag{45}$$

where

$$
\begin{aligned}
f(\kappa, q, \Delta) &= J_1(q)J_1(\kappa) \exp\left[-\frac{1}{4}R\kappa^2\right] \\
&\times \exp\left[-\frac{\theta_T^2}{4\theta_R^2\theta_\beta^2}\left(q^2\theta_\beta^2 + 4\theta_R^2\kappa^2 + 2\theta_\beta\theta_R q\kappa \cos\Delta\right)\right] \\
&\times \exp\left[\int_0^z dz W_o \alpha_t(z)\, G(q, \kappa, \Delta)\right],
\end{aligned} \tag{46}
$$

$$G(q, \kappa, \Delta) = \exp\left[\frac{-1}{4\alpha_p\theta_R^2\theta_\beta^2}\left(G_1(q, \kappa, \Delta) + G_2(q, \kappa, \Delta)\right)\right], \tag{47}$$

$$G_1(q, \kappa, \Delta) = \theta_\beta^2 q^2 + \theta_R^2\kappa^2\left(2 - \frac{z}{z_h}\right)^2 + 2\theta_\beta\theta_R q\kappa\left(2 - \frac{z}{z_h}\right)\cos\Delta \tag{48}$$

$$G_2(q, \kappa, \Delta) = \theta_\beta^2 q^2 + \theta_R^2\kappa^2\left(1 - \frac{z}{z_h}\right)^2 + 2\theta_\beta\theta_R q\kappa\left(1 - \frac{z}{z_h}\right)\cos\Delta \tag{49}$$

In these equations the following definitions are used:

61

$\kappa = |\vec{\kappa}|$,

$q = |\vec{q}|$,

Δ is the angle between $\vec{\kappa}$ and $\vec{q}$

$\theta_T = \eta/k\rho_T$ (transmitter beam spread),

$\theta_\beta = \rho_R/z_h$ (half angle subtended by receiver at z_h,

$\theta_R = \rho_T/\rho_R$,

ρ_T is the transmitter beam radius, and

J_1 is the first order Bessel function

In Eq. 45 the factor in front of the triple integral is the single scatter lidar result multiplied by z_h^2. For small optical depth $\left(\int_0^{z_h} \alpha dz \ll 1\right)$ the triple integral reduces to $1/z_h^2$.

Equation 45 has been programmed on an 80386 based computer. However, the calculation takes several hours and is not feasible to perform. Additional simplifications must be made for future work.

A Lidar Experiments at Dripping Spring, NM

A.1 Introduction

In June, 1988 lidar measurements, with the GL/OP low altitude lidar system, were made at Dripping Spring, New Mexico, a desert region approximately 80 miles south of Albuquerque. The GL/OP low altitude lidar system measured extinction coefficients and cloud heights during this field program.

Section A.2 discusses the data analysis techniques, results, and conclusions made from these measurements. Section A.3 discusses the minimum calculable extinction coefficient as a function of lidar parameters. We include this work here (instead of in Section 5) because it is a direct result of the difficulties we had in calculating the small extinction coefficients of the clear air of Dripping Spring.

A.2 Results and Conclusions

We successfully measured cloud heights during the field program. Backscattered power from clouds is easily identified during data taking either by the experimenter or by the data acquisition system software.

During clear air conditions extinction coefficients could not be determined because of the low backscattered power from the relatively clear air over the New Mexican desert. Instead, we show that the measured backscattered power agrees well with the theoretically expected backscattered power from a purely Rayleigh atmosphere. The total amount of backscattered power is due to Rayleigh scattering off of atmospheric molecules and to Mie scattering off of larger atmopsheric aerosols. The lowest amount of backscatter will always be equal to or greater than that due to Rayleigh scattering.

Although the lidar "sees" the backscattered power from a Rayleigh atmosphere, the amount is too low to be used to calculate extinction. The reason, which we discuss in the next section, is because the decrease in signal due to the "$1/r^2$" effect dominates that due to the extinction effect.

A standard Rayleigh atmosphere model was calculated for each of the days of the field trip using measured values of humidity, pressure, and temperature. The model provides values for the backscatter coefficient β_{Ray} and the extinction coefficient

α_{Ray} as a funciton of altitude z. The backscattered power P_{Ray} is then calculated in the following manner:

$$P_{Ray}(z) = \frac{\beta_{Ray}(z)}{z^2} \exp\left(-2\int_0^z \alpha_{Ray}(z)dz\right)$$

The measured backscattered power is known at discrete ranges along a path at some angle with respect to the horizontal. Each range point at which the backscattered power is measured is compared to the calculated backscattered power at the same altitude. If a calculated backscattered power for a given measured range interval does not exist then it is interpolated from the surrounding points where calculations were made. This is done up to an altitude of 15 km, the highest altitude considered in the model.

The lidar system is not absolutely calibrated and therefore only relative backscattered powers are known. The theoretical backscattered power is multiplied by a constant which is determined by linearly fitting it to the measured backscattered power at the initial range.

The lower curve labeled "data" in Fig. 25a is a lidar return with a cloud at 5 km. The air below 5 km is clear. The vertical axis for this curve corresponds to a number proportional to the measured backscattered power. The horizontal axis corresponds to the altitude above sea level. The lidar was pointing 35° above the horizontal for this return. Dripping Spring is 1.8 km above sea level.

The lower curve labeled "Rayleigh model" in Fig.25b is the theoretically calculated backscattered power assuming a Rayleigh atmosphere.

The upper curve in Fig. 25 is the ratio of lidar backscattered power to Rayleigh backscattered power. The vertical axis for this curve is just a dimensionless number. We see that the Rayleigh model predicts the backscattered power fairly well up to the cloud. The cloud produces backscattered power 100 times the level predicted by Rayleigh.

All other lidar returns for clear air conditions show similar agreement between data and Rayleigh model.
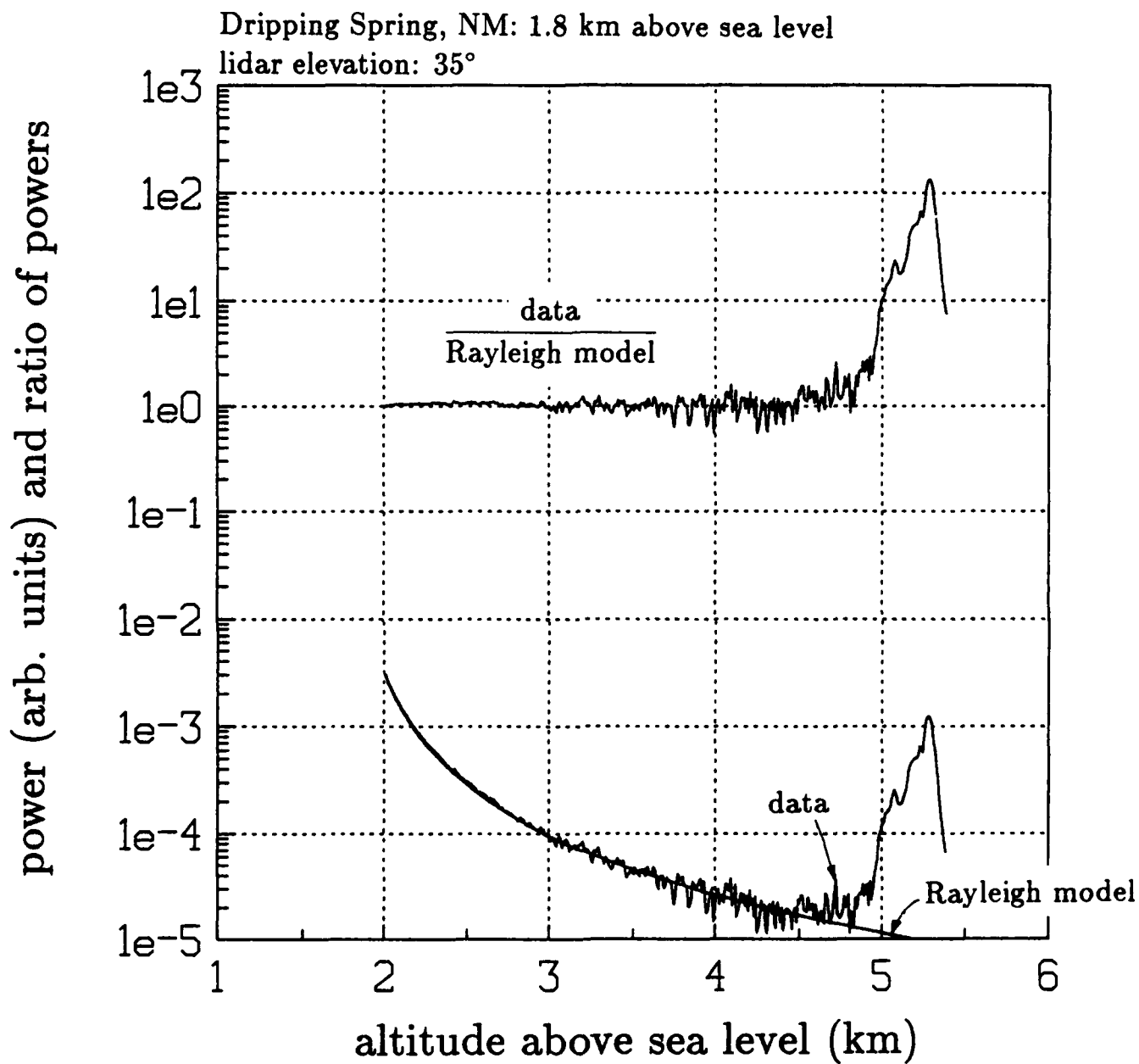
Dripping Spring, NM: 1.8 km above sea level
lidar elevation: 35°

$\dfrac{\text{data}}{\text{Rayleigh model}}$

data

Rayleigh model

power (arb. units) and ratio of powers

altitude above sea level (km)

Figure 25: Lower: lidar backscattered power (with a cloud) and Rayleigh model backscattered power. Upper: ratio of data to model.

A.3 Minimum Calculable Extinction

A.3.1 General Discussion

It is difficult to determine small values of extinction coefficient ($\alpha < 0.1$ km^{-1}) from lidar data, even if there is no noise. This difficulty arises because the decrease of the lidar return is nearly the same as its decrease due to the $1/r^2$ effect alone (assuming constant extinction and backscatter coefficient). This effect is more severe for near ranges; it is easier to measure small extinction coefficients at far ranges, if the return signal is large enough.

The lidar return $P(r)$ for constant extinction coefficient α and constant backscatter coefficient (in units for which the backscatter coefficient is one) is

$$P(r) = P(r_o)\frac{r_o^2}{r^2} \exp\left[-2\alpha\left(r - r_o\right)\right] \tag{50}$$

where r_o is a reference range where the lidar return is known to be $P(r_o)$. The decrease of the lidar return with the $1/r^2$ effect alone is expressed as

$$P_{r^2} = P(r_o)\frac{r_o^2}{r^2} \tag{51}$$

To to detect the extinction effect the lidar receiver must be sensitive to signals of at least the order of $P_{r^2} - P$. Figure 26 shows a plot of $\delta = (P_{r^2} - P)/P(r_o)$ versus range for different values of extinction, with $r_o = 0.25$ km. Figure 27 shows δ versus range for different values of r_o, with $\alpha = 0.015$ km^{-1}.

Figure 26 shows that for Rayleigh scattering ($\alpha \approx 0.015$ km^{-1}) the maximum value of δ is approximately 2×10^{-3} times the power at the reference position. This amount of power is difficult to measure if the reference power is in the range of sensitivity of the detector; photomultiplier tubes operating in current mode are typically only sensitive to approximately three orders of magnitude of signal. This amount of power could be measured if the detector were set to be saturated by the reference power.

Figure 27, however, shows that the effect is not as severe if the reference range is increased. This is because the $1/r^2$ effect is determined by the ratio of two range values, while the extinction is determined by the difference of two range values. The
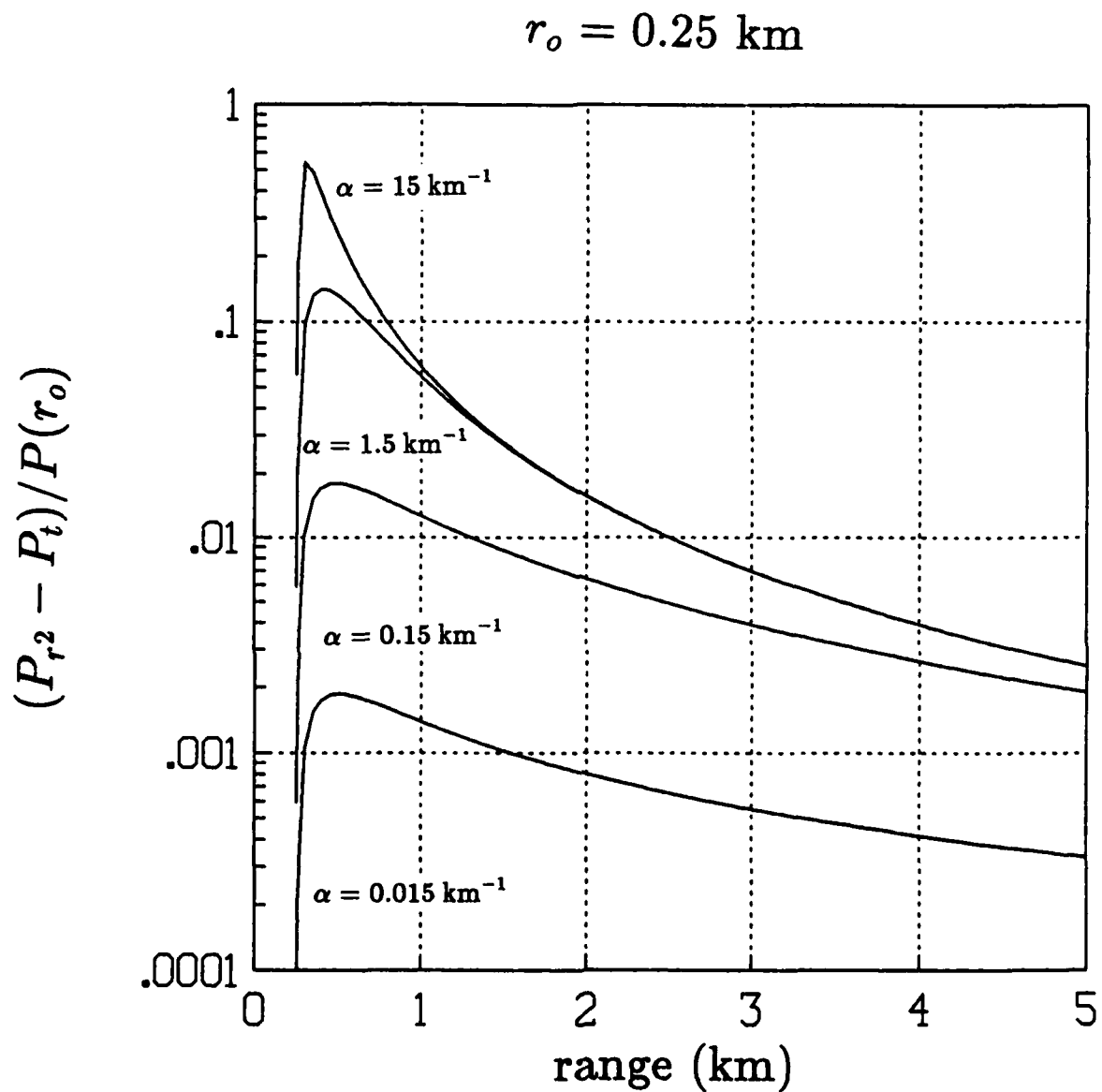
$$r_o = 0.25 \text{ km}$$

Figure 26: Difference between lidar returns with and without decrease due to extinction. Returns are equal at $r_o = 0.25$ km.
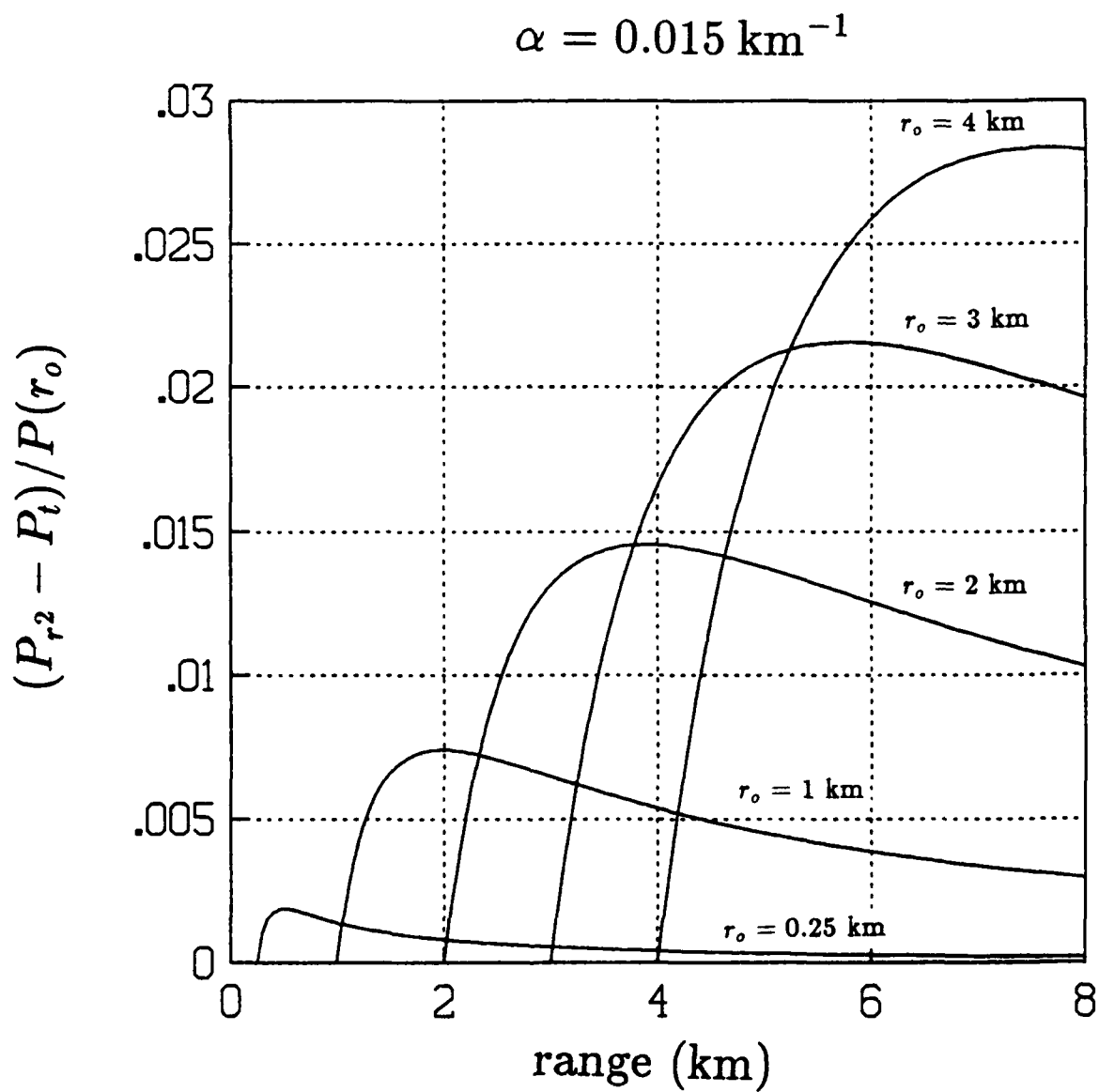
Figure 27: Difference between lidar returns with and without decrease due to extinction, for different r_o, with $\alpha = 0.015 \ \text{km}^{-1}$.
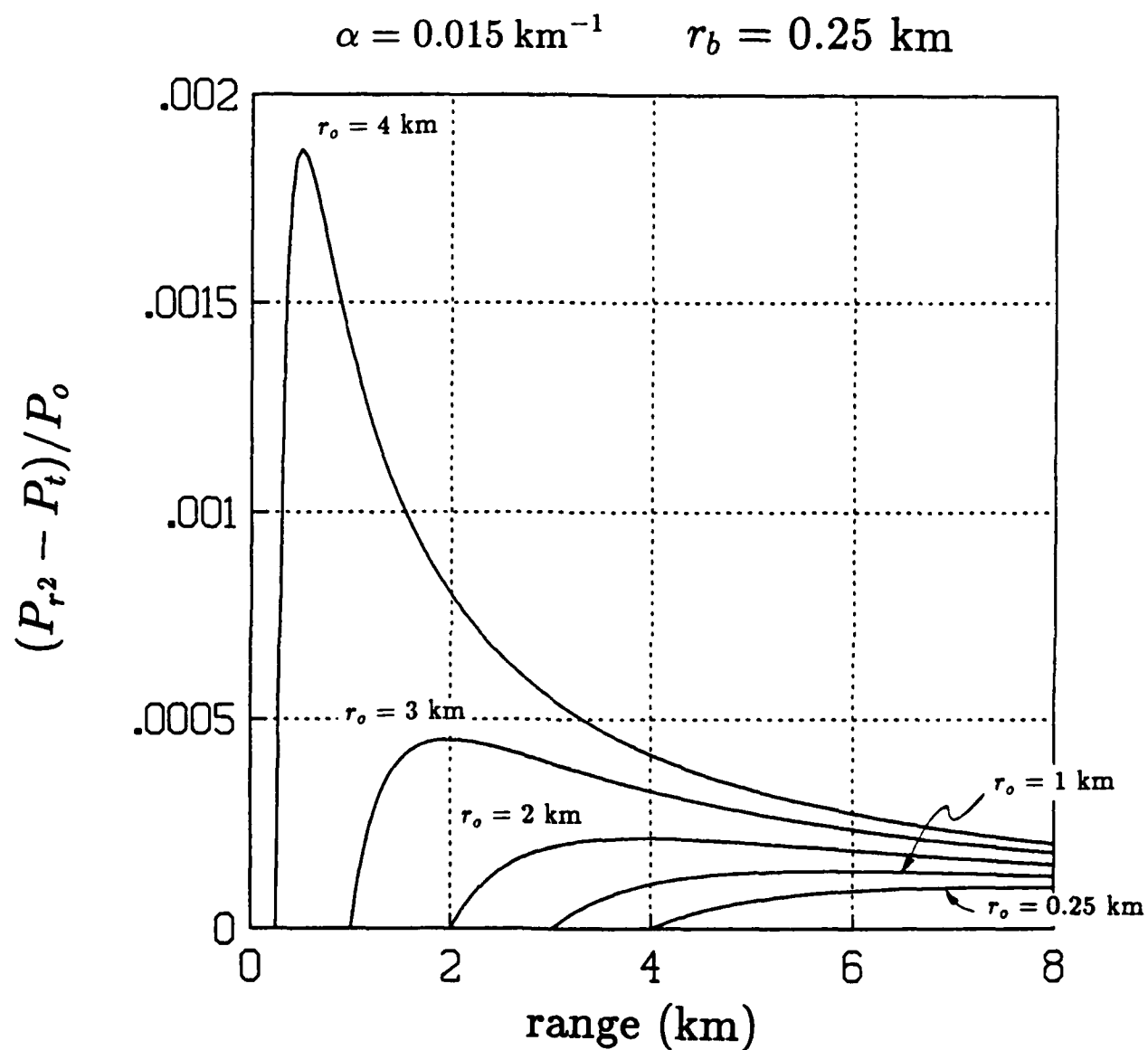
Figure 28: Difference between lidar returns with and without decrease due to extinction. Values at different r_o decrease as $1/r_o^2$.

ratio of two range values (r_1/r_2, where $r_1 < r_2$) increases as the range increases, if the difference between the two ranges remains constant.

Unfortunately, moving the reference range out may not help matters because the reference power may become quite small. This is shown in Fig. 28, which is a plot of $\delta' = (P_{r^2} - P)/P_o$. P_o is the lidar return at an initial range and is defined by

$$P(r_o) = P_o \frac{r_b^2}{r_o^2} \exp\left[-2\alpha\left(r_o - r_b\right)\right] \tag{52}$$

where r_b is chosen to be 0.25 km.

A.3.2 Application to Lidar Data

The above discussion implies that we cannot determine extinction coefficients from the lidar data taken during clear air conditions at Dripping Spring. Previously we concluded, by comparing the data to a Rayleigh model, that the extinction coefficient during clear air conditions is primarily due to Rayleigh scattering and is typically less than 0.02 km^{-1}.

The lidar detector was always set so that the return signal at 0.25 km range was within the sensitive range of the photomultiplier tube. The maximum output of the photomultiplier tube, in its linear regime of operation, is 500 mV (into a 50Ω load). For clear air conditions the maximum photomultiplier output (at maximum gain) would be typically 300 mV. Figure 28 then indicates that greater than 0.018×300 mV = 0.54 mV changes in the lidar return should have been detectable to differentiate between extinction and $1/r^2$ effects. However, a change of one bit in the analog-to-digital converter corresponds to 0.49 mV (12 bits over 2 Volts). Also, fluctuations due to noise and background were typically two to three bits.

The problem could not be alleviated by increasing the photomultiplier anode-to-cathode voltage. During clear air conditions this voltage was always set to its maximum suggested value.

We could have alleviated the problem by increasing the gain of the amplifier which precedes the analog-to-digital converter, thus saturating the photomultiplier at 0.25 km. However, since the noise fluctuations increase by the same factor as the signal, averaging over a greater number of laser shots would have been necessary.

The noise fluctuations decrease linearly with the square root of the number of laser shots. Thus, increasing the gain by a factor of two would mean that four times as many laser pulses would have to be averaged over to get the same amount of noise.

References

[1] C.F. Bohren and D.R. Huffman, *Absorption and Scattering of Light by Small Particles*, John Wiley & Sons (1983).

[2] M. Born and E. Wolf, *Principles of Optics*, 6th edition, Pergamon Press (1980).

[3] G. Mie, *Ann. D. Physik* 25, 377-445 (1908).

[4] R.M. Measures, *Laser Remote Sensing*, John Wiley & Sons (1984).

[5] C.E. Junge, *Air Chemistry and Radioactivity*, Academic Press (1963).

[6] D. Deirmendjian, "Scattering and Polarizaton Properties of Water Clouds and Hazes in the Visible and Infrared," *Applied Optics* 2, 187–196 (1964).

[7] D. Deirmendjian, *Electromagnetic Scattering on Spherical Polydispersions*, American Elsevier (1969).

[8] J.D. Klett, "Stable Analytical Inversion solution for Processing Lidar Returns", *Applied Optics* 20, 211–220 (1981).

[9] W.H. Press, B.P. Flannery, S.A Teukolsky, and W.T. Vetterling, *Numerical Recipes in C*, Cambridge University Press (1988).

[10] G.G. Koenig (GL/OP), private communciation.

[11] A. Ishimaru *Wave Propagation and Scattering in Random Media, Vol. 1*, Academic Press (1978).